

MedReasoner: Reinforcement Learning Drives Reasoning Grounding from Clinical Thought to Pixel-Level Precision

Zhonghao Yan^{1*}, Muxi Diao^{12*}, Yuxuan Yang¹, Ruoyan Jing¹, Jiayuan Xu¹, Kaizhou Zhang¹,
Lele Yang¹, Yanxi Liu³, Kongming Liang^{1†}, Zhanyu Ma¹

¹Beijing University of Posts and Telecommunications

²Zhongguancun Academy

³Beijing Information Science and Technology University

{zhonghao.yan, dmx, liangkongming}@bupt.edu.cn
https://pris-cv.github.io/MedReasoner.github.io/

Abstract

Accurately grounding regions of interest (ROIs) is critical for diagnosis and treatment planning in medical imaging. While multimodal large language models (MLLMs) combine visual perception with natural language, current medical-grounding pipelines still rely on supervised fine-tuning with explicit spatial hints, making them ill-equipped to handle the implicit queries common in clinical practice. This work makes three core contributions. We first define **Unified Medical Reasoning Grounding (UMRG)**, a novel vision–language task that demands clinical reasoning and pixel-level grounding. Second, we release **U-MRG-14K**, a dataset of 14K samples featuring pixel-level masks alongside implicit clinical queries and reasoning traces, spanning 10 modalities, 15 super-categories, and 108 specific categories. Finally, we introduce **MedReasoner**, a modular framework that distinctly separates reasoning from segmentation: an MLLM reasoner is optimized with reinforcement learning, while a frozen segmentation expert converts spatial prompts into masks, with alignment achieved through format and accuracy rewards. MedReasoner achieves state-of-the-art performance on U-MRG-14K and demonstrates strong generalization to unseen clinical queries, underscoring the significant promise of reinforcement learning for interpretable medical grounding.

1 Introduction

Medical imaging plays a central role in modern healthcare, where clinicians routinely examine regions of interest (ROIs) within these images to assess the health of organs and tissues (Cheng et al. 2023; Lin et al. 2024; Yan et al. 2025). Consequently, precise object detection and image segmentation (often called **grounding**) are essential for tasks such as disease diagnosis and treatment planning (Chen et al. 2021; Ma et al. 2024). To further enhance diagnostic efficiency and interpretability, medical Multimodal Large Language Models (MLLMs) have recently emerged (Li et al. 2023a; Chen et al. 2024a; Xu et al. 2025). These models integrate visual

perception with language interaction, allowing them to accept free-form language queries, generate high-quality responses, and even identify queried ROIs.

Despite these significant advances, a crucial limitation persists: **MLLM outputs remain at the image level**. To translate reasoning into visual outputs, every language reference must be grounded to a spatial location. However, while expert models (Cheng et al. 2023; Yue et al. 2024) achieve high grounding accuracy, they rely on precise spatial prompts (e.g., *bounding boxes* and *points*). Such detailed annotations are rarely provided by clinicians in real workflows (see Fig. 1 for an example query). Recent MLLMs attempt to move beyond handcrafted prompts by coupling rich visual components (Da et al. 2024; Huang et al. 2025b). However, existing medical grounding pipelines are still trained in a fully supervised manner on explicitly phrased referring expressions (e.g., “*segment the left lung*”) (Liu et al. 2023; Koleilat et al. 2024). Collecting such finely annotated data is costly and, more importantly, misaligned with real clinical queries, which are often **implicit** (e.g., “*What can be inferred from the irregular shadow?*”). Although some models can name anatomical structures, they often fail to ground them (see Fig. 1). Therefore, we need models with reasoning that can turn implicit clinical phrases into explicit spatial targets for grounding in clinical scenarios.

Existing medical visual–question answering (VQA) datasets (Lau et al. 2018; He et al. 2020; Liu et al. 2021) evaluate semantic understanding with image-level question–answer pairs but lack spatial labels. Conversely, large-scale segmentation datasets (Ye et al. 2023; Zhao et al. 2024; Li et al. 2024b) provide pixel-accurate masks yet omit language annotations. Neither class of dataset addresses the implicit queries that arise in real clinical practice. **We have no principled way to measure whether a framework can translate implicit clinical queries into precise spatial grounding**. Here, we are particularly interested in two research questions that must be addressed before implicit clinical queries can be grounded reliably:

- **RQ1:** *How can we create data that mirrors clinicians’ implicit query patterns while still providing the pixel-level annotations needed for training and evaluation?*

*These authors contributed equally.

†Corresponding Author

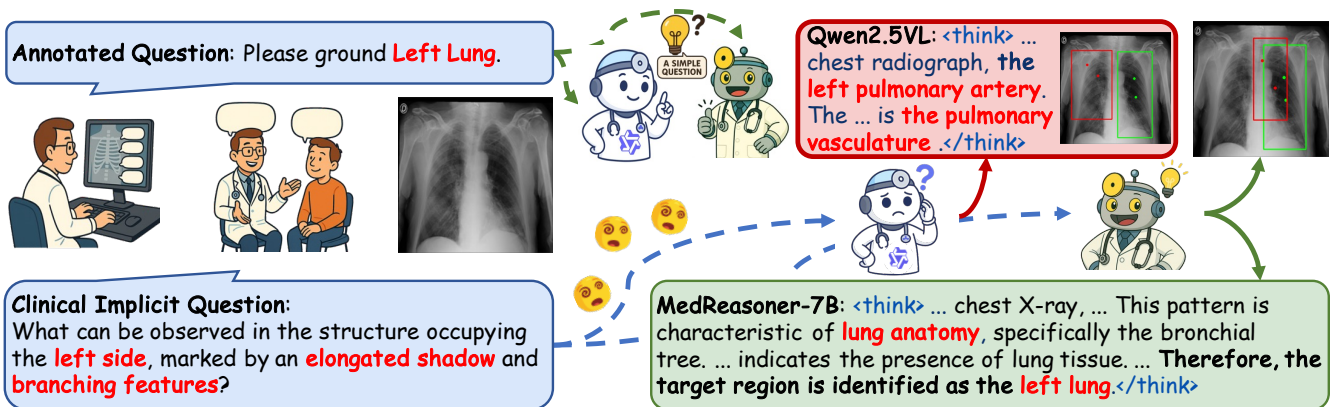


Figure 1: Comparison of annotated question and implicit clinical question. The ground-truth bounding box is green, and models’ predicted box is red. **MedReasoner** precisely identifies the target with the reasoning trace and achieves accurate grounding.

- **RQ2:** How can we enable models to interpret implicit clinical queries and accurately ground the corresponding image regions without handcrafted spatial prompts?

Guided by the research questions above, we formally introduce the **Unified Medical Reasoning Grounding (UMRG)** task. UMRG demands a framework that integrates linguistic reasoning with spatial grounding. To succeed, a framework need: (1) interpret the implicit query, (2) reason over visual cues and anatomical priors to infer the latent target, and (3) generate the accurate pixel-level grounding of that ROIs. This three-stage process mirrors how clinicians inspect images, reflect, and mark ROIs. Full task specifications are given in Section 4.1.

In response to **RQ1**, we propose **U-MRG-14K**, a rigorously curated dataset of 14K high-quality samples tailored to the UMRG task. U-MRG-14K is constructed from three open-source datasets. To generate semantically rich and clinically meaningful supervision, we employ GPT-4o (OpenAI 2024) as a simulator of clinician behavior. And we design a three-stage prompting pipeline that yields high-quality QA pairs, including implicit queries, chain-of-thought (CoT) reasoning traces, and final grounding steps for each target region. Further construction details appear in Section 3.

In response to **RQ2**, we present **MedReasoner**, a reinforcement learning (RL) framework for medical reasoning and grounding. MedReasoner is decoupled into two plug-and-play components: **Clinical Reasoning Module (CRM)**, any MLLM that reasons over implicit queries and generates lightweight spatial prompts (a bounding box plus two key points); **Anatomical Segmentation Module (ASM)**, any model that accepts these prompts and returns a pixel-level mask. Because CRM and ASM exchange minimal geometric cues, they can be upgraded without retraining the other. Most existing grounding pipelines rely on supervised finetuning (SFT) with special tokens (Lai et al. 2024; Tong et al. 2025). This approach suffers from: (1) **annotation hunger**, it requires large, heavily annotated datasets and CoT traces are especially costly; and (2) **phrase overfitting**, it encourages models to echo explicit referring phrases and fails to develop genuine reasoning ability. MedReasoner solve these

weaknesses through a rule-based RL training scheme that optimizes only the CRM. In each step, the CRM produces a *think* trace and an *answer* containing spatial prompts, and the frozen ASM renders a mask. Rewards for output format and spatial accuracy drive exploration, gradually aligning reasoning with precise grounding and achieving state-of-the-art performance on U-MRG-14K. As shown in Fig. 1, the RL-driven MedReasoner yields sharper grounding and more coherent reasoning than an instruction-tuned baseline, demonstrating its superiority on implicit-query grounding.

To summarize, our contributions are as follows:

- We formulate the **UMRG** task and propose **U-MRG-14K**. U-MRG-14K pairs implicit clinical queries with pixel-level masks and includes CoT traces to improve the interpretability of grounding.
- We present **MedReasoner**, an RL-driven, plug-and-play framework in which the CRM and the ASM are fully decoupled. This design enables easy substitution and extension to future models and clinical modalities.
- We demonstrate through extensive empirical evaluations the effectiveness of our proven MedReasoner framework. We will release the code, and dataset for future research.

2 Related Work

2.1 MLLMs for Medical Image Analysis

Recent advancements in MLLMs have significantly enhanced their capabilities for medical image analysis, with contributions from visual-language alignment techniques (Zhu et al. 2025; Wang et al. 2024; Bai et al. 2025; Guo et al. 2025). These progressions have been further extended to various medical applications, including the integration of visual expert modules into pre-trained language models (Li et al. 2023a; Sellergren et al. 2025), and the unification of medical understanding and generation through heterogeneous knowledge adaptation and general foundation models (Chen et al. 2024a; Lin et al. 2025; Xu et al. 2025). However, significant gaps remain in their handling of clinical complexities and crucial clinical grounding tasks, which have seen limited exploration.

2.2 Visual Grounding with Medical Reasoning

Recent MLLMs have demonstrated powerful reasoning capabilities (OpenAI 2024; Guo et al. 2025; Liu et al. 2025; Zhu et al. 2025; Bai et al. 2025). For visual grounding in general-purpose images, these models often leverage segmentation tools like SAM (Kirillov et al. 2023), with methods ranging from training new tokens (Lai et al. 2024; Ren et al. 2024) to prompting for geometric outputs (Chen et al. 2024c; Uesato et al. 2022). However, direct application in medical scenarios is challenging due to opaque reasoning and noisy data. While some specialized works have attempted to address this (Huang et al. 2025b; Trinh et al. 2025; Luo et al. 2024; Li et al. 2025), they often struggle with the natural language found in clinical practice. Inspired by Seg-Zero (Uesato et al. 2022), we employ reinforcement learning to generate an explicit CoT (Wei et al. 2022). This approach enhances medical visual grounding performance while offering a transparent reasoning process, thereby increasing trust in clinical applications.

3 U-MRG-14K Dataset

3.1 Data Generation

Most existing medical imaging datasets treat visual-grounding and VQA as separate tasks. As a result, some models support natural-language interaction without pixel-level analysis, whereas the accuracy of mainstream segmentation models hinges on the precision of supplied visual prompts. MoCoVQA (Huang et al. 2025a) attempts to unify the two tasks, yet its questions use explicit phrasing that fails to reflect the ambiguity common in routine clinical practice.

To address this gap, we construct **U-MRG-14K**, a medical grounding dataset centered on implicit referential expressions. U-MRG-14K is generated with GPT-4o (OpenAI 2024) through carefully designed prompts. As shown in Fig. 2, its generation process has three stages.

Stage 1: Dataset Preprocessing. We collect 14K image-mask pairs from SA-Med2D-20M (Ye et al. 2023), BiomedParse (Zhao et al. 2024), and IMIS-Bench (Cheng et al. 2025). We then standardize and complete the *super-category* labels (coarse anatomical regions) and *category* labels (specific organs or lesions) from the source datasets, producing a consistent and reliable taxonomy. The dataset comprises 15 super-categories and 108 categories. Table 1 provides a systematic comparison showing the advantages of U-MRG-14K over existing datasets.

Stage 2: Descriptions & QA Formats Generation. To facilitate the creation of high-quality QA pairs, we perform two preparatory steps. First, for each image, we generate two complementary descriptions: (i) a **short description** capturing the visual appearance of the region in plain and intuitive language, and (ii) a **long description** providing a medically precise interpretation of the target area. Second, we use GPT-4o to design a set of QA formats for each super-category. The *questions* mimic realistic clinical queries with vague or implicit references, while the *answers* provide a step-by-step, clinical reasoning path for correct grounding.

Dataset	# Prompts	QAs	Sup.	Cat.	CoT
SA-Med2D	20M	✗	-	219	✗
BioMedParse	1.1M	✗	3	82	✗
IMED	361M	✗	6	204	✗
MoCoVQA	100K	✓	-	-	✗
U-MRG-14K	14K	✓	15	108	✓

Table 1: Comparison of U-MRG-14K with existing medical vision-language datasets. **Sup.** and **Cat.** denote the numbers of *super-categories* and fine-grained *categories*, respectively. U-MRG-14K supplies customized QA templates for each category, and is the only dataset that includes CoT annotations for reasoning-aware evaluation.

On average, we create about 20 formats per super-category, with the exact number manually adjusted for class diversity.

Stage 3: QA Pairs Construction. Using the per-image descriptions and super-category QA formats from Stage 2, we prompt GPT-4o to synthesize instance-level QA pairs. Each answer contains an explicit, step-by-step reasoning trace guiding the model from an under-specified query to the correct spatial grounding, thereby enhancing interpretability and enabling manual verification. Prompts are iteratively refined, and all generated QA pairs undergo manual screening to remove factual inconsistencies or misaligned reasoning. U-MRG-14K is the first medical-image grounding dataset that includes both pixel-level annotations and complete CoT reasoning traces, providing a valuable resource for reasoning-based grounding and implicit-query QA tasks.

All generated QA pairs were manually reviewed to eliminate duplicates and factual inconsistencies. Further details and examples of the procedure are provided in Appendix B.

3.2 Dataset statistics

U-MRG-14K contains 14K image-mask pairs from ten imaging modalities (e.g., *CT*, *MRI*). The dataset is organized into 15 super-categories (e.g., *abdomen*, *lung*) covering frequent anatomical regions and pathology-oriented classes, providing broad clinical coverage. Within these, 108 fine-grained categories denote specific structures, reflecting hierarchical structure of anatomy. For instance, *left lung* and *right lung* are separate categories nested under the *lung* super-category. Beyond pixel-level masks, every sample includes a CoT reasoning trace. These annotations make the reasoning process transparent and verifiable, allowing researchers to inspect the model’s decision path.

We implemented a stringent three-phase manual quality control process for U-MRG-14K. Initially, 5 graduate-level students with medical imaging knowledge performed data deduplication and fact-checking, with each entry reviewed by 3 individuals. Subsequently, we conducted a detailed review, focusing on eliminating clinically illogical CoT data. Finally, 2 experienced radiologists with over 5 years of practice performed a random audit of 10% of the data to quantify overall quality. Comprehensive data statistics are in Appendix B.4.

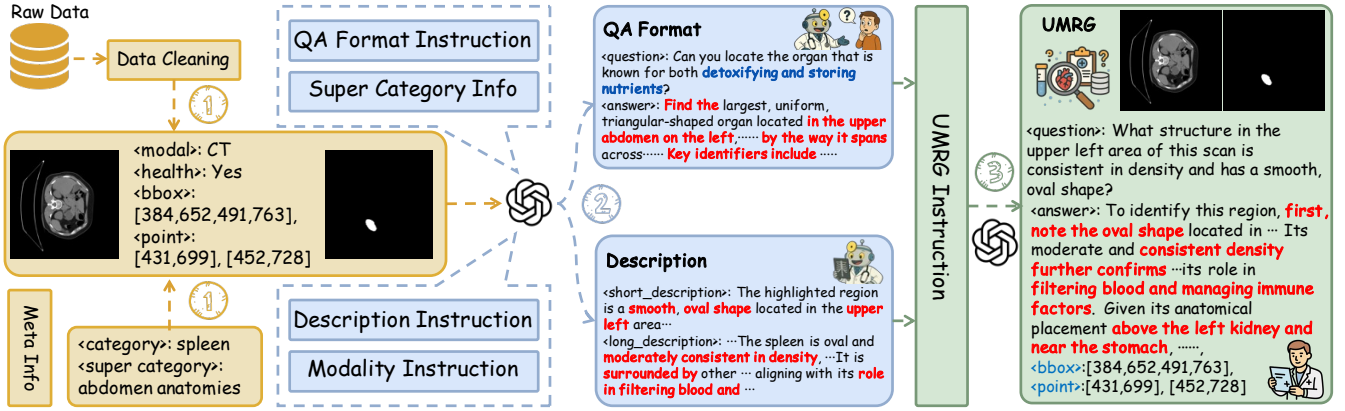


Figure 2: Overview of the **U-MRG-14K** construction pipeline: (1) Data cleaning and metadata organization manually, (2) Description and QA format generation via GPT-4o, (3) QA pair generation with GPT-4o and human verification.

4 MedReasoner

4.1 Task Definition

Given a medical image \mathcal{I} and a clinical query \mathcal{Q} with implicit referring expressions, the model \mathbf{G} outputs a bounding box \mathcal{B} , two semantic key points \mathcal{P}_1 and \mathcal{P}_2 , and a pixel-level segmentation mask \mathcal{M} . The process can be formulated as:

$$\{\mathcal{T}, \mathcal{B}, \mathcal{P}_1, \mathcal{P}_2, \mathcal{M}\} = \mathbf{G}(\mathcal{I}, \mathcal{Q}). \quad (1)$$

where \mathcal{T} is an optional CoT trace that records the model’s intermediate reasoning, analogous to how a clinician infers the target from implicit linguistic cues.

4.2 Model Architecture

Enabling native pixel-level segmentation in an MLLM usually requires custom `[MASK]` tokens, multi-head decoders, and large collections of manual mask annotations (Pi et al. 2024; Lai et al. 2024; Tong et al. 2025). However, MedSAM2 (Ma et al. 2025) already yields modality-agnostic masks out of the box. As shown in Fig. 3, **MedReasoner** decouples language reasoning from pixel-level grounding, thereby (1) mitigating phrase over-fitting to enable authentic reasoning, and (2) treating MedSAM-family models as plug-and-play components controllable by language.

Clinical Reasoning Module. We employ Lingshu (Xu et al. 2025) as our **Clinical Reasoning Module (CRM)** \mathbf{F}_{reason} . Given $(\mathcal{I}, \mathcal{Q})$, CRM outputs a structured tuple `<think>...<think><answer>` $\mathcal{B}, \mathcal{P}_1, \mathcal{P}_2$ `<answer>`. A bounding box \mathcal{B} is often inadequate in medical images: boxes may enclose multiple organs or lesions, and their corners lack semantics for SAM-style prompts. We therefore add two key points $\mathcal{P}_1, \mathcal{P}_2$ on visually distinctive regions. These enrich spatial cues at low annotation cost. To learn reliable cues without compromising linguistic competence, we train \mathbf{F}_{reason} with **Group Relative Policy Optimization (GRPO)** (Shao et al. 2024), using: (1) **format rewards** enforcing the output schema, and (2) **accuracy rewards** measuring spatial correctness.

Anatomical Segmentation Module. We instantiate the Anatomical Segmentation Module (ASM) with a frozen MedSAM2 (Ma et al. 2025), denoted as \mathbf{F}_{seg} . The tuple $(\mathcal{B}, \mathcal{P}_1, \mathcal{P}_2)$ produced by the CRM is fed to \mathbf{F}_{seg} , which transforms these coarse prompts into a high-resolution mask \mathcal{M} without any task-specific fine-tuning. Freezing \mathbf{F}_{seg} preserves MedSAM2’s strong zero-shot delineation ability, while allowing \mathbf{F}_{reason} to concentrate on language understanding and spatial reasoning.

4.3 Reward Functions

Reward functions in RL guide a model toward the behaviors we desire. For UMRG, we introduce three rewards that first prompt the model to reason about the implicit target and then to predict the bounding box and key points.

Reasoning Formats Reward. This reward evaluates the structural validity of the model’s output, focusing on the formatting of the reasoning and answer components. It assigns \mathbb{R}_{think} to assess whether the model produces a well-structured `<think>` block, and \mathbb{R}_{answer} to verify whether the `<answer>` block is a valid JSON object containing the required fields: `bbox`, `points_1`, and `points_2`. These rewards do not evaluate the correctness or quality of the reasoning content itself, but rather the presence and structural completeness of the expected formats. Both \mathbb{R}_{think} and \mathbb{R}_{answer} are assigned discrete values in the range $[0, 1]$.

Grounding Box Reward. This reward evaluates the quality of the predicted bounding box $\mathcal{B}_p = [x_1^p, y_1^p, x_2^p, y_2^p]$ against the ground-truth box $\mathcal{B}_g = [x_1^g, y_1^g, x_2^g, y_2^g]$, where all coordinates are normalized to $[0, 1]$. First, the **IoU reward** measures the spatial overlap between two boxes:

$$\mathbb{R}_{iou} = \frac{\text{Area}(\mathcal{B}_p \cap \mathcal{B}_g)}{\text{Area}(\mathcal{B}_p \cup \mathcal{B}_g)}. \quad (2)$$

Second, the **Alignment reward** computes the average L1 distance between corresponding corner coordinates, normal-

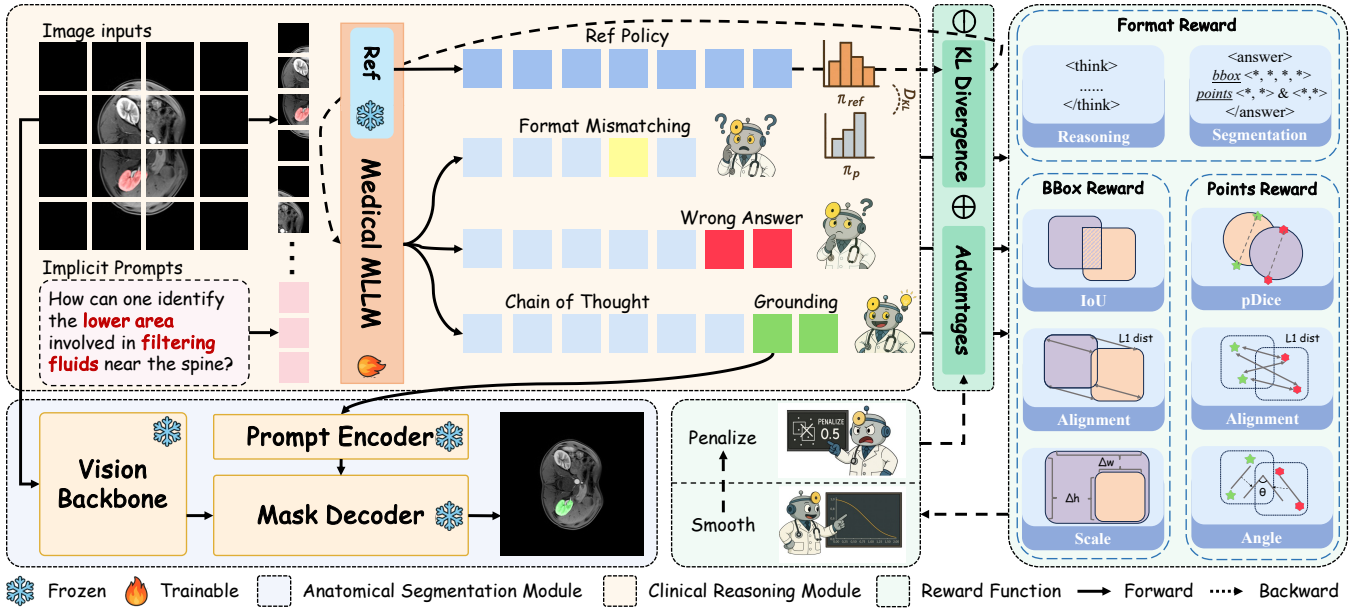


Figure 3: Overview of the **MedReasoner** framework. MedReasoner transforms implicit clinical prompts into pixel-level grounding via a two-stage process. The **CRM** first generates intermediate reasoning and grounding outputs (*CoT*, *bounding box*, and *key points*). Then, the **ASM** converts the grounded outputs into final segmentation masks.

ized by the diagonal of \mathcal{B}_g :

$$\mathbb{R}_{\text{align}} = \frac{1}{4} \sum_{i=1}^4 \left| \mathcal{B}_p^{(i)} - \mathcal{B}_g^{(i)} \right|. \quad (3)$$

Third, the **Scale reward** captures shape consistency in terms of area and aspect ratio. Specifically, we compute the logarithmic difference in box area and aspect ratio, and define:

$$\mathbb{R}_{\text{scale}} = \sqrt{(\Delta \log A)^2 + (\Delta \log R)^2}, \quad (4)$$

where A denotes box area and R the aspect ratio. Smaller values indicate better structural alignment.

Grounding Points Reward. This reward evaluates the quality of the predicted key point pair $\mathcal{P}_p = \{\mathbf{p}_1^p, \mathbf{p}_2^p\}$ by comparing it with the ground-truth pair $\mathcal{P}_g = \{\mathbf{p}_1^g, \mathbf{p}_2^g\}$, where each point $\mathbf{p} = (x, y)$ is normalized to $[0, 1]$. First, the **pDice reward** estimates the spatial overlap between circles formed by each point pair. Each uses the two points as diameter endpoints, and the Dice score is computed as:

$$\mathbb{R}_{\text{pdice}} = \frac{2 \cdot \text{Area}(O_p \cap O_g)}{\text{Area}(O_p) + \text{Area}(O_g)}, \quad (5)$$

where O_p and O_g are the circles constructed from \mathcal{P}_p and \mathcal{P}_g , respectively. Second, the **Alignment reward** computes the mean absolute error between corresponding points:

$$\mathbb{R}_{\text{align}} = \frac{1}{2} \sum_{i=1}^2 (|x_i^p - x_i^g| + |y_i^p - y_i^g|). \quad (6)$$

Third, the **Angle reward** measures the cosine similarity between the predicted and ground-truth direction vectors, capturing angular consistency:

$$\mathbb{R}_{\text{angle}} = |\cos(\theta)| = \left| \frac{\langle \mathbf{v}_p, \mathbf{v}_g \rangle}{\|\mathbf{v}_p\|_2 \cdot \|\mathbf{v}_g\|_2} \right|, \quad (7)$$

where $\mathbf{v}_p = \mathbf{p}_2^p - \mathbf{p}_1^p$ and $\mathbf{v}_g = \mathbf{p}_2^g - \mathbf{p}_1^g$. Further details of reward functions are provided in Appendix C.3.

Smoothing and Penalization. To enhance training stability and differentiate prediction quality, we apply smoothing functions to all reward components. For the \mathbb{R}_{iou} , $\mathbb{R}_{\text{pdice}}$ and $\mathbb{R}_{\text{angle}}$ rewards, we use logarithmic smoothing:

$$\mathcal{S}_{\log}(r; k) = \frac{\log(kr + 1)}{\log(k + 1)}, \quad (8)$$

where $r \in [0, 1]$ is the raw reward and k is a scaling factor (default $k = 3$). For the $\mathbb{R}_{\text{align}}$ and $\mathbb{R}_{\text{scale}}$ rewards, we use exponential smoothing:

$$\mathcal{S}_{\text{exp}}(d; k, c) = \frac{1}{1 + e^{k(d-c)}}, \quad (9)$$

where $d \in [0, 2]$ is the normalized distance, and c is the target center (default $c = 1$).

After smoothing, we apply a penalization function $\mathcal{N}(\cdot)$ to softly down-weight unreliable predictions. For each reward, two validity scores are computed to reflect the spatial plausibility of the output. The final reward is adjusted as:

$$\mathcal{N}(r; v_1, v_2) = \lambda r + (1 - \lambda)r \cdot \frac{v_1 + v_2}{2}, \quad (10)$$

where r is the smoothed reward, v_1 and v_2 are the two validity scores, and $\lambda = 0.7$ by default. More details of smoothing and penalization are provided in Appendix C.4.

5 Experiments

5.1 Experimental Settings

Models. We conduct a comprehensive comparison across a wide range of models. For general MLLMs, we utilized

Method	IoU \uparrow	pDice \uparrow	Dice \uparrow	Super-Categories (IoU \uparrow)									
				Abd.	Brain	Eye	Heart	Hist.	Lung	Ves.	Neo.	N-Neo.	Inf.
General MLLMs													
GPT-4o	2.65	1.12	4.72	0.92	0.91	3.29	0.36	2.8	11.70	1.83	1.01	4.16	6.37
Gemini-2.5-flash	7.86	3.24	14.29	3.99	5.69	6.39	7.77	6.63	16.37	9.08	7.15	13.91	11.4
Qwen2.5VL-7B	12.61	7.14	22.73	6.84	<u>23.97</u>	29.35	8.37	9.22	20.79	20.46	8.00	24.97	19.4
InternVL3-8B	5.70	2.46	9.23	3.72	6.54	2.02	3.67	5.56	14.44	7.88	3.78	8.71	9.00
Qwen2.5-VL-72B	<u>18.32</u>	<u>12.39</u>	<u>29.71</u>	<u>13.60</u>	20.06	38.3	<u>15.51</u>	8.74	<u>35.25</u>	20.64	<u>20.69</u>	<u>30.19</u>	16.92
InternVL3-78B	4.02	1.55	7.23	2.04	2.95	2.33	2.12	6.12	12.21	4.19	1.33	8.19	5.62
Medical-Specific MLLMs													
MedR1-2B	8.18	3.60	14.73	3.53	12.55	1.10	3.53	8.14	25.58	8.81	4.39	13.57	17.35
MiniInternVL-4B	2.88	0.85	4.76	1.88	2.67	0.68	1.60	3.45	7.99	3.59	1.56	3.76	6.59
MedGamma-4B	5.39	1.90	8.90	4.23	6.92	1.28	3.41	4.78	17.22	6.92	3.17	3.90	10.04
HuatuogPT-7B	10.13	5.23	19.76	5.88	18.16	3.88	6.63	9.56	22.94	15.58	8.25	16.12	15.87
Lingshu-7B	8.19	3.73	16.48	4.03	15.72	6.97	6.27	8.06	19.77	8.63	6.34	13.31	11.99
Chiron-o1-8B	6.40	2.46	10.05	3.82	6.90	4.29	4.20	5.99	12.86	9.50	5.53	11.31	10.86
Grounding-Specific MLLMs													
VLMR1-REC-3B	13.96	-	22.19	8.64	21.81	25.09	8.19	<u>10.69</u>	29.77	<u>21.35</u>	8.76	26.59	21.41
SegZero-7B	16.14	5.23	26.05	11.66	23.37	<u>40.23</u>	13.12	9.35	22.18	20.68	12.58	29.46	<u>21.93</u>
SAM4MLLM-8B	7.94	-	16.49	6.30	14.69	5.09	5.81	7.46	12.61	11.99	6.24	11.96	12.40
MedReasoner-7B	32.42	26.55	37.78	30.27	32.81	51.50	34.72	11.66	50.75	29.91	33.58	37.19	30.48

Table 2: Results on the **U-MRG-14K** test set under the **MedReasoner** paradigm. Each candidate uses one medical MLLM as the **CRM** to output a bounding box and two key points; the **ASM** is fixed to *MedSAM2*. **Bold** numbers denote the best score in each column, and underlined numbers denote the second best.

GPT-4o (OpenAI 2024), Gemini-2.5-flash (Google 2025), Qwen2.5VL-7B/72B (Bai et al. 2025) and InternVL3-8B/78B (Zhu et al. 2025). For medical-specific MLLMs, we selected MedR1-2B (Lai et al. 2025), MiniInternVL-4B (Gao et al. 2024), MedGamma-4B (Sellersgren et al. 2025), HuatuogPT-7B-Qwen2.5VL (Chen et al. 2024a), Lingshu-7B (Xu et al. 2025), and Chiron-o1-8B (Sun et al. 2025). For segmentation models, we chose MedSAM (Ma et al. 2024), SAM-Med2D (Cheng et al. 2023) and MedSAM2 (Ma et al. 2025). For grounding-specific models, we included SAM4MLLM (Chen et al. 2024c), VLMR1-REC-3B (Shen et al. 2025) and SegZero-7B (Liu et al. 2025).

Datasets. We train MedReasoner on U-MRG-14K, using the data preparation strategy mentioned in Section 3.1. We randomly hold out 2.5K samples as a test set, and use the remaining data for training. All quantitative results reported in this paper are obtained on the test set.

Implementation Details. We adopt Lingshu-7B with the Soft reward function as our default CRM and default ASM to MedSAM2 (see details in Appendix D.1).

Evaluation Metrics. We compute three evaluation metrics: **IoU**, **pDice**, and **Dice** to assess model performance. **IoU** measures the bounding box localization accuracy predicted by MLLMs. **pDice** quantifies keypoint pair semantic alignment by evaluating the overlap of circles formed by predicted endpoints (formally defined in Section 4.3). **Dice** assesses segmentation quality based on masks generated by downstream models conditioned on MLLM outputs.

5.2 Medical Reasoning Grounding Results

For fair comparison, we evaluated models under the MedReasoner paradigm, using a single MLLM as CRM to return bounding box and key point, with MedSAM2 fixed as ASM. All MLLMs are driven by the same user prompt (full prompt in Appendix C.2). As shown in Table 2, MedReasoner-7B achieved superior overall performance, significantly leading the second-best Qwen2.5VL-72B by 14.10 in IoU, 14.16 in pDice, and 8.07 in Dice. This highlights its precise spatial prompting capability. While General MLLMs, such as GPT-4o (IoU 2.65), and Medical-Specific MLLMs, like HuatuogPT-7B (IoU 10.13), demonstrated cross-modal understanding or domain benefits, they consistently lacked the fine-grained precision required for UMRG. In contrast, MedReasoner-7B established a substantial lead among Grounding-Specific MLLMs, surpassing SegZero-7B (IoU 16.14) by over 16 IoU points, validating our RL-driven grounding strategy for accurate regional prompt translation. This superiority extended across super-categories, with MedReasoner-7B leading in most (e.g., Lung’s IoU was 50.75, Eye’s IoU was 51.50), though all models, including ours, faced challenges in complex categories like Histology (MedReasoner-7B’s IoU was 11.66).

5.3 Ablation Study

We conduct ablation studies to verify our proposed design’s effectiveness. All experiments are trained on U-MRG-14K and use the same user prompt during inference.

Effect of Reward Types. This ablation study investigated how reward design influences RL training for CRM. Our

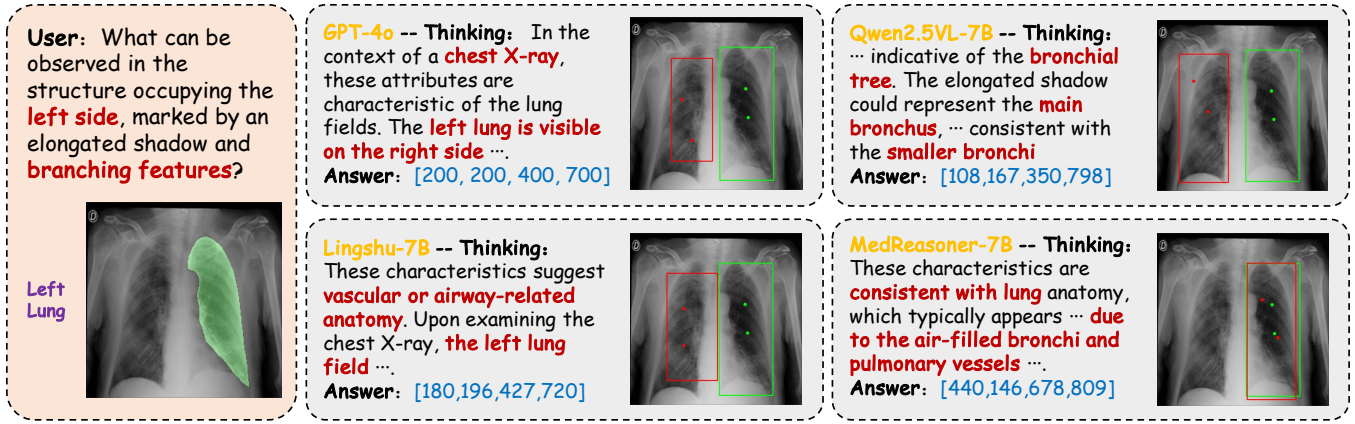


Figure 4: Open-source (**Qwen2.5VL-7B**), closed-source (**GPT-4o**), and medically post-trained (**Lingshu-7B**) models reason and specify referents within CoT processes, a characteristic tied to their respective training methodologies. Our **MedReasoner-7B** integrates grounding information during training, thereby aligning pixel-level grounding with semantic-level understanding.

Method	IoU \uparrow	pDice \uparrow	Dice \uparrow	# Ref. \downarrow
Lingshu	8.19	3.73	16.51	2
Lingshu w/ SFT	9.15	2.88	15.22	2
Lingshu w/ RL(Base)	15.85	8.29	28.79	0
Lingshu w/ RL(Hard)	<u>31.69</u>	<u>24.36</u>	<u>33.51</u>	0
Lingshu w/ RL(Soft)	32.42	26.55	37.78	0

Table 3: Comparison of the **SFT** baseline with three RL variants: **Base**, **Hard**, and **Soft** on U-MRG-14K. **# Ref.** denotes refusals to ground answers with the reasoning prompt.

Method	Dice \uparrow		
	w/ Points	w/ BBox	BBox & Points
MedSAM	5.67	28.39	19.00
SAM-Med2D	<u>33.23</u>	<u>35.03</u>	<u>36.48</u>
MedSAM2	34.86	37.15	37.78

Table 4: Dice scores for three segmentation backbones under three prompt types: **key points only**, **bounding box only**, and the **combined bounding box & points**.

SFT baseline had a low IoU of 9.15 and 2 query refusals (as Table 3 shows). RL fine-tuning drastically improved performance, eliminating all refusals. We evaluated three reward variants: **Base** (a hard-threshold scheme (Liu et al. 2025)), **Hard** (our full reward), and **Soft** (IoU and pDice only). While Base removed refusals, its IoU of 15.85 was considerably lower. Our Hard reward significantly outperformed Base, increasing IoU by 15.84 points. The Soft reward variant achieved the best overall IoU of 32.42, surpassing Hard by 0.73 points, suggesting that less strict alignment fosters better exploration and more accurate grounding solutions.

Effect of Segmentation Backbones. This ablation assesses the ASM. Table 4 reports results for three medical SAM variants: MedSAM, SAM-Med2D, and MedSAM2.

Method	Reason	IoU \uparrow	pDice \uparrow	# Ref. \downarrow
Qwen2.5VL-7B	\times	14.57	8.14	13
Qwen2.5VL-7B	\checkmark	12.61	7.14	0
Lingshu-7B	\times	9.35	2.40	4
Lingshu-7B	\checkmark	8.19	3.73	2
MedReasoner-7B	\times	<u>30.29</u>	<u>25.82</u>	12
MedReasoner-7B	\checkmark	32.42	26.55	0

Table 5: Impact of adding an explicit reasoning step vs. a direct prompt for three CRMs. **Reason** indicates whether the model is prompted to reason first (\checkmark) or respond directly (\times).

To investigate prompt influence, we evaluated three input formats per backbone: points only, bounding box only, and the combined bounding box and points. The combination consistently yielded the best Dice (37.78), with MedSAM2 achieving the highest performance across all configurations.

Effect of Reasoning Strategies. This ablation tests whether prompting the model to reason before grounding helps when answering implicit queries. We designed two user prompts (see Appendix C.2): **Direct** asks the CRM to output the spatial prompt immediately, whereas **Reasoning** instructs it to first generate a brief CoT. As Table 5 shows, the Reasoning prompt significantly reduces refusal rates compared to the Direct prompt. While base Qwen2.5VL and Lingshu exhibit a slight performance drop due to their limited inherent reasoning capabilities, this behavior is expected. However, after CRM training within the MedReasoner framework, the Reasoning strategy clearly outperforms the Direct one. This confirms that an explicit reasoning phase is valuable for implicit-query grounding.

5.4 Qualitative Results

Figure 4 compares four MLLMs' predictions on a chest X-ray query requiring implicit reasoning. **GPT-4o** produces a coherent CoT and an accurate image-level answer, but its spatial output is wrong: the bounding box is misplaced

and coordinates are rounded, indicating limited fine-grained grounding. **Qwen2.5VL-7B** fails at the reasoning stage, resulting in an incorrect diagnosis and an irrelevant box. **Lingshu-7B** correctly identifies the *left lung* but misplaces the box, demonstrating that it alone doesn't guarantee accurate localization. Only **MedReasoner-7B** precisely identifies and pinpoints the target; its box tightly encloses the bronchial tree of the left lung, with key points aligning to it. These observations highlight the necessity of explicit RL-based grounding. It preserves the reasoning quality of large models while enforcing the spatial precision crucial for UMRG. Additional qualitative results are in Appendix D.4.

6 Conclusion

We present the **UMRG** task, which challenges models to transform implicit clinical queries into precise pixel-level grounding. To support this, we introduce **U-MRG-14K**, a large-scale dataset featuring rich annotations and reasoning traces. To solve UMRG, we propose **MedReasoner**, a modular framework that decouples reasoning from segmentation and leverages RL to align linguistic reasoning with spatial precision. Extensive experiments demonstrate that MedReasoner consistently outperforms existing models in accuracy. We believe this framework offers a promising step toward trustworthy and generalizable medical grounding systems.

References

- Bai, S.; Chen, K.; Liu, X.; Wang, J.; Ge, W.; Song, S.; Dang, K.; Wang, P.; Wang, S.; Tang, J.; Zhong, H.; Zhu, Y.; Yang, M.; Li, Z.; Wan, J.; Wang, P.; Ding, W.; Fu, Z.; Xu, Y.; Ye, J.; Zhang, X.; Xie, T.; Cheng, Z.; Zhang, H.; Yang, Z.; Xu, H.; and Lin, J. 2025. Qwen2.5-VL Technical Report. *arXiv preprint arXiv:2502.13923*.
- Chen, J.; Gui, C.; Ouyang, R.; Gao, A.; Chen, S.; Chen, G. H.; Wang, X.; Zhang, R.; Cai, Z.; Ji, K.; et al. 2024a. Huatuoqpt-vision, towards injecting medical visual knowledge into multimodal llms at scale. *arXiv preprint arXiv:2406.19280*.
- Chen, J.; Lu, Y.; Yu, Q.; Luo, X.; Adeli, E.; Wang, Y.; Lu, L.; Yuille, A. L.; and Zhou, Y. 2021. Transunet: Transformers make strong encoders for medical image segmentation. *arXiv preprint arXiv:2102.04306*.
- Chen, Y.; Wei, M.; Zheng, Z.; Hu, J.; Shi, Y.; Xiong, S.; Zhu, X. X.; and Mou, L. 2024b. Causalclipseg: Unlocking clip's potential in referring medical image segmentation with causal intervention. In *International Conference on Medical Image Computing and Computer-Assisted Intervention*, 77–87. Springer.
- Chen, Y.-C.; Li, W.-H.; Sun, C.; Wang, Y.-C. F.; and Chen, C.-S. 2024c. Sam4mllm: Enhance multi-modal large language model for referring expression segmentation. In *European Conference on Computer Vision*, 323–340. Springer.
- Chen, Z.; Wu, J.; Wang, W.; Su, W.; Chen, G.; Xing, S.; Zhong, M.; Zhang, Q.; Zhu, X.; Lu, L.; et al. 2024d. Internvl: Scaling up vision foundation models and aligning for generic visual-linguistic tasks. In *Proceedings of the IEEE/CVF Conference on Computer Vision and Pattern Recognition*, 24185–24198.
- Cheng, J.; Fu, B.; Ye, J.; Wang, G.; Li, T.; Wang, H.; Li, R.; Yao, H.; Cheng, J.; Li, J.; et al. 2025. Interactive medical image segmentation: A benchmark dataset and baseline. In *Proceedings of the Computer Vision and Pattern Recognition Conference*, 20841–20851.
- Cheng, J.; Ye, J.; Deng, Z.; Chen, J.; Li, T.; Wang, H.; Su, Y.; Huang, Z.; Chen, J.; Jiang, L.; Sun, H.; He, J.; Zhang, S.; Zhu, M.; and Qiao, Y. 2023. SAM-Med2D. *arXiv:2308.16184*.
- Da, L.; Wang, R.; Xu, X.; Bhatia, P.; Kass-Hout, T.; Wei, H.; and Xiao, C. 2024. Segment as You Wish—Free-Form Language-Based Segmentation for Medical Images. *arXiv preprint arXiv:2410.12831*.
- Diao, M.; Li, R.; Liu, S.; Liao, G.; Wang, J.; Cai, X.; and Xu, W. 2025a. Seas: Self-evolving adversarial safety optimization for large language models. In *Proceedings of the AAAI Conference on Artificial Intelligence*, volume 39, 23778–23786.
- Diao, M.; Yang, L.; Yin, H.; Wang, Z.; Wang, Y.; Tian, D.; Liang, K.; and Ma, Z. 2025b. DriveRX: A Vision-Language Reasoning Model for Cross-Task Autonomous Driving. *arXiv preprint arXiv:2505.20665*.
- Gao, Z.; Chen, Z.; Cui, E.; Ren, Y.; Wang, W.; Zhu, J.; Tian, H.; Ye, S.; He, J.; Zhu, X.; et al. 2024. Mini-internvl: A flexible-transfer pocket multimodal model with 5% parameters and 90% performance. *arXiv preprint arXiv:2410.16261*.
- Google. 2025. Gemini-2.5-Flash. Online; GA release.
- Guo, D.; Yang, D.; Zhang, H.; Song, J.; Zhang, R.; Xu, R.; Zhu, Q.; Ma, S.; Wang, P.; Bi, X.; et al. 2025. Deepseek-r1: Incentivizing reasoning capability in llms via reinforcement learning. *arXiv preprint arXiv:2501.12948*.
- He, X.; Zhang, Y.; Mou, L.; Xing, E.; and Xie, P. 2020. Pathvqa: 30000+ questions for medical visual question answering. *arXiv preprint arXiv:2003.10286*.
- Hu, J.; Li, Y.; Sun, H.; Song, Y.; Zhang, C.; Lin, L.; and Chen, Y.-W. 2024. Lga: A language guide adapter for advancing the sam model's capabilities in medical image segmentation. In *International Conference on Medical Image Computing and Computer-Assisted Intervention*, 610–620. Springer.
- Hu, R.; Rohrbach, M.; and Darrell, T. 2016. Segmentation from natural language expressions. In *European conference on computer vision*, 108–124. Springer.
- Huang, X.; Li, H.; Cao, M.; Chen, L.; You, C.; and An, D. 2024. Cross-modal conditioned reconstruction for language-guided medical image segmentation. *IEEE Transactions on Medical Imaging*.
- Huang, X.; Shen, L.; Liu, J.; Shang, F.; Li, H.; Huang, H.; and Yang, Y. 2025a. Towards a multimodal large language model with pixel-level insight for biomedicine. In *Proceedings of the AAAI Conference on Artificial Intelligence*, volume 39, 3779–3787.
- Huang, Y.; Peng, Z.; Zhao, Y.; Yang, P.; Yang, X.; and Shen, W. 2025b. MedSeg-R: Reasoning Segmentation in Medical Images with Multimodal Large Language Models. *arXiv preprint arXiv:2506.10465*.

- Kirillov, A.; Mintun, E.; Ravi, N.; Mao, H.; Rolland, C.; Gustafson, L.; Xiao, T.; Whitehead, S.; Berg, A. C.; Lo, W.-Y.; et al. 2023. Segment anything. In *Proceedings of the IEEE/CVF international conference on computer vision*, 4015–4026.
- Koleilat, T.; Asgariandehkordi, H.; Rivaz, H.; and Xiao, Y. 2024. Medclip-sam: Bridging text and image towards universal medical image segmentation. In *International conference on medical image computing and computer-assisted intervention*, 643–653. Springer.
- Lai, X.; Tian, Z.; Chen, Y.; Li, Y.; Yuan, Y.; Liu, S.; and Jia, J. 2024. Lisa: Reasoning segmentation via large language model. In *Proceedings of the IEEE/CVF Conference on Computer Vision and Pattern Recognition*, 9579–9589.
- Lai, Y.; Zhong, J.; Li, M.; Zhao, S.; and Yang, X. 2025. Med-r1: Reinforcement learning for generalizable medical reasoning in vision-language models. *arXiv preprint arXiv:2503.13939*.
- Lau, J. J.; Gayen, S.; Ben Abacha, A.; and Demner-Fushman, D. 2018. A dataset of clinically generated visual questions and answers about radiology images. *Scientific data*, 5(1): 1–10.
- Li, C.; Wong, C.; Zhang, S.; Usuyama, N.; Liu, H.; Yang, J.; Naumann, T.; Poon, H.; and Gao, J. 2023a. Llavamed: Training a large language-and-vision assistant for biomedicine in one day. *Advances in Neural Information Processing Systems*, 36: 28541–28564.
- Li, J.; Liu, C.; Bai, W.; Arcucci, R.; Bercea, C. I.; and Schnabel, J. A. 2025. Enhancing Abnormality Grounding for Vision Language Models with Knowledge Descriptions. *arXiv preprint arXiv:2503.03278*.
- Li, M.; Meng, M.; Ye, S.; Fulham, M.; Bi, L.; and Kim, J. 2024a. Language-guided Medical Image Segmentation with Target-informed Multi-level Contrastive Alignments. *arXiv preprint arXiv:2412.13533*.
- Li, W.; Qu, C.; Chen, X.; Bassi, P. R.; Shi, Y.; Lai, Y.; Yu, Q.; Xue, H.; Chen, Y.; Lin, X.; et al. 2024b. Abdomenatlas: A large-scale, detailed-annotated, & multi-center dataset for efficient transfer learning and open algorithmic benchmarking. *Medical Image Analysis*, 97: 103285.
- Li, Z.; Li, Y.; Li, Q.; Wang, P.; Guo, D.; Lu, L.; Jin, D.; Zhang, Y.; and Hong, Q. 2023b. Lvit: language meets vision transformer in medical image segmentation. *IEEE transactions on medical imaging*, 43(1): 96–107.
- Lin, T.; Chen, Z.; Yan, Z.; Yu, W.; and Zheng, F. 2024. Stable diffusion segmentation for biomedical images with single-step reverse process. In *International Conference on Medical Image Computing and Computer-Assisted Intervention*, 656–666. Springer.
- Lin, T.; Zhang, W.; Li, S.; Yuan, Y.; Yu, B.; Li, H.; He, W.; Jiang, H.; Li, M.; Song, X.; et al. 2025. Healthgpt: A medical large vision-language model for unifying comprehension and generation via heterogeneous knowledge adaptation. *arXiv preprint arXiv:2502.09838*.
- Liu, B.; Zhan, L.-M.; Xu, L.; Ma, L.; Yang, Y.; and Wu, X.-M. 2021. Slake: A semantically-labeled knowledge-enhanced dataset for medical visual question answering. In *2021 IEEE 18th international symposium on biomedical imaging (ISBI)*, 1650–1654. IEEE.
- Liu, J.; Zhang, Y.; Chen, J.-N.; Xiao, J.; Lu, Y.; A Landman, B.; Yuan, Y.; Yuille, A.; Tang, Y.; and Zhou, Z. 2023. Clip-driven universal model for organ segmentation and tumor detection. In *Proceedings of the IEEE/CVF international conference on computer vision*, 21152–21164.
- Liu, Y.; Peng, B.; Zhong, Z.; Yue, Z.; Lu, F.; Yu, B.; and Jia, J. 2025. Seg-zero: Reasoning-chain guided segmentation via cognitive reinforcement. *arXiv preprint arXiv:2503.06520*.
- Luo, L.; Tang, B.; Chen, X.; Han, R.; and Chen, T. 2024. Vividmed: Vision language model with versatile visual grounding for medicine. *arXiv preprint arXiv:2410.12694*.
- Ma, J.; He, Y.; Li, F.; Han, L.; You, C.; and Wang, B. 2024. Segment anything in medical images. *Nature Communications*, 15(1): 654.
- Ma, J.; Yang, Z.; Kim, S.; Chen, B.; Baharoon, M.; Fallahpour, A.; Asakereh, R.; Lyu, H.; and Wang, B. 2025. Medsam2: Segment anything in 3d medical images and videos. *arXiv preprint arXiv:2504.03600*.
- OpenAI. 2024. GPT-4o (GPT-4 Omni). Online.
- OpenAI. 2024. OpenAI o1. <https://openai.com/o1/>.
- Pi, R.; Yao, L.; Gao, J.; Zhang, J.; and Zhang, T. 2024. Perceptiongpt: Effectively fusing visual perception into llm. In *Proceedings of the IEEE/CVF conference on computer vision and pattern recognition*, 27124–27133.
- Qiao, R.; Tan, Q.; Dong, G.; MinhuiWu, M.; Sun, C.; Song, X.; Wang, J.; Gongque, Z.; Lei, S.; Zhang, Y.; et al. 2025. We-math: Does your large multimodal model achieve human-like mathematical reasoning? In *Proceedings of the 63rd Annual Meeting of the Association for Computational Linguistics (Volume 1: Long Papers)*, 20023–20070.
- Rasheed, H.; Maaz, M.; Shaji, S.; Shaker, A.; Khan, S.; Cholakkal, H.; Anwer, R. M.; Xing, E.; Yang, M.-H.; and Khan, F. S. 2024. Glamm: Pixel grounding large multimodal model. In *Proceedings of the IEEE/CVF Conference on Computer Vision and Pattern Recognition*, 13009–13018.
- Ren, Z.; Huang, Z.; Wei, Y.; Zhao, Y.; Fu, D.; Feng, J.; and Jin, X. 2024. Pixellm: Pixel reasoning with large multimodal model. In *Proceedings of the IEEE/CVF Conference on Computer Vision and Pattern Recognition*, 26374–26383.
- Sellergren, A.; Kazemzadeh, S.; Jaroensri, T.; Kiraly, A.; Traverse, M.; Kohlberger, T.; Xu, S.; Jamil, F.; Hughes, C.; Lau, C.; et al. 2025. MedGemma Technical Report. *arXiv preprint arXiv:2507.05201*.
- Shao, Z.; Wang, P.; Zhu, Q.; Xu, R.; Song, J.; Bi, X.; Zhang, H.; Zhang, M.; Li, Y.; Wu, Y.; et al. 2024. Deepseekmath: Pushing the limits of mathematical reasoning in open language models. *arXiv preprint arXiv:2402.03300*.
- Shen, H.; Liu, P.; Li, J.; Fang, C.; Ma, Y.; Liao, J.; Shen, Q.; Zhang, Z.; Zhao, K.; Zhang, Q.; et al. 2025. Vlm-r1: A stable and generalizable r1-style large vision-language model. *arXiv preprint arXiv:2504.07615*.
- Sheng, G.; Zhang, C.; Ye, Z.; Wu, X.; Zhang, W.; Zhang, R.; Peng, Y.; Lin, H.; and Wu, C. 2025. Hybridflow: A flexible and efficient rlhf framework. In *Proceedings of*

- the *Twentieth European Conference on Computer Systems*, 1279–1297.
- Song, X.; Diao, M.; Dong, G.; Wang, Z.; Fu, Y.; Qiao, R.; Wang, Z.; Fu, D.; Wu, H.; Liang, B.; et al. 2024. Cs-bench: A comprehensive benchmark for large language models towards computer science mastery. *arXiv preprint arXiv:2406.08587*.
- Sun, H.; Jiang, Y.; Lou, W.; Zhang, Y.; Li, W.; Wang, L.; Liu, M.; Liu, L.; and Wang, X. 2025. Enhancing Step-by-Step and Verifiable Medical Reasoning in MLLMs. *arXiv preprint arXiv:2506.16962*.
- Tong, Q.; Lu, Z.; Liu, J.; Zheng, Y.; and Lu, Z. 2025. MediSee: Reasoning-based Pixel-level Perception in Medical Images. *arXiv preprint arXiv:2504.11008*.
- Trinh, Q.-H.; Nguyen, M.-V.; Peng, J.; Bagci, U.; and Jha, D. 2025. PRS-Med: Position Reasoning Segmentation with Vision-Language Model in Medical Imaging. *arXiv preprint arXiv:2505.11872*.
- Uesato, J.; Kushman, N.; Kumar, R.; Song, F.; Siegel, N.; Wang, L.; Creswell, A.; Irving, G.; and Higgins, I. 2022. Solving math word problems with process-and outcome-based feedback. *arXiv preprint arXiv:2211.14275*.
- Wang, W.; Lv, Q.; Yu, W.; Hong, W.; Qi, J.; Wang, Y.; Ji, J.; Yang, Z.; Zhao, L.; XiXuan, S.; et al. 2024. Cogvlm: Visual expert for pretrained language models. *Advances in Neural Information Processing Systems*, 37: 121475–121499.
- Wang, X.; Diao, M.; Liu, Y.; Wang, C.; Liang, K.; Ma, Z.; and Guo, J. 2025a. Harnessing Caption Detailness for Data-Efficient Text-to-Image Generation. *arXiv preprint arXiv:2505.15172*.
- Wang, X.; Xu, S.; Shan, X.; Zhang, Y.; Diao, M.; Duan, X.; Huang, Y.; Liang, K.; and Ma, Z. 2025b. CineTechBench: A Benchmark for Cinematographic Technique Understanding and Generation. *arXiv preprint arXiv:2505.15145*.
- Wang, Z.; Lu, Y.; Li, Q.; Tao, X.; Guo, Y.; Gong, M.; and Liu, T. 2022. Cris: Clip-driven referring image segmentation. In *Proceedings of the IEEE/CVF conference on computer vision and pattern recognition*, 11686–11695.
- Wei, J.; Wang, X.; Schuurmans, D.; Bosma, M.; Xia, F.; Chi, E.; Le, Q. V.; Zhou, D.; et al. 2022. Chain-of-thought prompting elicits reasoning in large language models. *Advances in neural information processing systems*, 35: 24824–24837.
- Xie, Y.; Zhou, T.; Zhou, Y.; and Chen, G. 2024. Simtxtseg: Weakly-supervised medical image segmentation with simple text cues. In *International Conference on Medical Image Computing and Computer-Assisted Intervention*, 634–644. Springer.
- Xu, W.; Chan, H. P.; Li, L.; Aljunied, M.; Yuan, R.; Wang, J.; Xiao, C.; Chen, G.; Liu, C.; Li, Z.; et al. 2025. Lingshu: A Generalist Foundation Model for Unified Multimodal Medical Understanding and Reasoning. *arXiv preprint arXiv:2506.07044*.
- Yan, Z.; Yin, Z.; Lin, T.; Zeng, X.; Liang, K.; and Ma, Z. 2025. PGP-SAM: Prototype-Guided Prompt Learning for Efficient Few-Shot Medical Image Segmentation. In *2025 IEEE 22nd International Symposium on Biomedical Imaging (ISBI)*, 1–5. IEEE.
- Yang, Z.; Wang, J.; Tang, Y.; Chen, K.; Zhao, H.; and Torr, P. H. 2022. Lavt: Language-aware vision transformer for referring image segmentation. In *Proceedings of the IEEE/CVF conference on computer vision and pattern recognition*, 18155–18165.
- Ye, J.; Cheng, J.; Chen, J.; Deng, Z.; Li, T.; Wang, H.; Su, Y.; Huang, Z.; Chen, J.; Jiang, L.; et al. 2023. Sa-med2d-20m dataset: Segment anything in 2d medical imaging with 20 million masks. *arXiv preprint arXiv:2311.11969*.
- Yue, W.; Zhang, J.; Hu, K.; Xia, Y.; Luo, J.; and Wang, Z. 2024. SurgicalSAM: Efficient class promptable surgical instrument segmentation. In *Proceedings of the AAAI Conference on Artificial Intelligence*, volume 38, 6890–6898.
- Zhao, T.; Gu, Y.; Yang, J.; Usuyama, N.; Lee, H. H.; Naumann, T.; Gao, J.; Crabtree, A.; Abel, J.; Moung-Wen, C.; et al. 2024. BiomedParse: a biomedical foundation model for image parsing of everything everywhere all at once. *arXiv preprint arXiv:2405.12971*.
- Zhu, J.; Wang, W.; Chen, Z.; Liu, Z.; Ye, S.; Gu, L.; Tian, H.; Duan, Y.; Su, W.; Shao, J.; et al. 2025. Internvl3: Exploring advanced training and test-time recipes for open-source multimodal models. *arXiv preprint arXiv:2504.10479*.

A More Details on UMRG Task

A.1 Referring Image Segmentation

Referring Image Segmentation (RIS) aims to segment a specific object within an image according to a natural language expression. First introduced in (Hu, Rohrbach, and Darrell 2016), RIS addresses the need for fine-grained, language-driven visual understanding, enabling users to interact with visual systems in a more intuitive and flexible manner. Unlike traditional segmentation tasks, RIS supports flexible object descriptions, enabling intuitive interaction.

Formally, the RIS task can be defined as follows: given an image $I \in \mathbb{R}^{H \times W \times 3}$ and a natural language expression $Q = \{q_1, q_2, \dots, q_n\}$, the goal is to predict a binary segmentation mask $M \in \{0, 1\}^{H \times W}$ that identifies the region corresponding to the object referred to by Q . Recent methods fall into three main categories:

Explicit Language Reasoning. This line of work narrows the language-vision gap by generating reasoning chains from text. LISA (Lai et al. 2024) introduces reasoning supervision via a frozen LLM and achieves strong zero-shot performance, but its token-level reasoning and reliance on supervision limit generalization. Seg-Zero (Liu et al. 2025) improves on this with a decoupled architecture trained by reinforcement learning, enabling explicit reasoning and superior performance without annotated reasoning data.

Fine-grained Cross-modal Alignment. These methods improve pixel-text alignment via fine-grained feature interactions. CRIS (Wang et al. 2022) employs contrastive learning for region-expression alignment but struggles with hard negatives and compositional queries. LAVT (Yang et al. 2022) enhances cross-modal encoding via early fusion, though its rigid architecture limits flexibility. GLaMM (Rasheed et al. 2024) enables multi-turn pixel-level grounding but requires extensive pretraining and infrastructure, hindering adaptability.

Foundation Model Augmentation. This category integrates general-purpose segmentation models for enhanced control. SAM4MLLM (Chen et al. 2024c) integrates SAM with a MLLM through refinement modules, improving mask accuracy though still limited by semantic misalignment.

A.2 Language-Guided Medical Image Segmentation

Language-Guided Medical Image Segmentation (LGMIS) aims to segment anatomical structures or pathological regions in medical images based on natural language instructions. It supports flexible expressions across modalities.

Given a medical image $I \in \mathbb{R}^{H \times W \times C}$, typically grayscale or multi-channel (e.g., CT, MRI), and a clinical instruction $Q = \{q_1, q_2, \dots, q_n\}$, the objective is to generate a segmentation mask $M \in \{0, 1\}^{H \times W}$ that delineates anatomical or pathological structures referenced by Q . Existing methods fall into two key categories:

Prompt Generation and Geometric Awareness. To support interactive and context-sensitive segmentation, some

methods generate language prompts dynamically and enforce geometric consistency. FLaNS (Da et al. 2024) uses retrieval-augmented prompts with a geometry-aware model for orientation-consistent segmentations. Besides, CLIP-based models (Liu et al. 2023) inject general language priors to support zero-shot anatomical segmentation.

Foundation Model Integration. Another line of research enhances LGMIS by combining pretrained vision-language and segmentation models under weak or zero-shot supervision. MedCLIP-SAM (Koleilat et al. 2024) fuses BiomedCLIP and SAM with ScoreCAM-based supervision to achieve weakly supervised yet accurate segmentation.

A.3 Referring Lesion Segmentation

Referring Lesion Segmentation (RLS) aims to identify lesion regions in medical images based on natural language descriptions. Compared to RIS, RLS presents unique challenges: the complexity of medical terminology, irregular lesion morphology, and the often vague nature of clinical language. Solving this task requires precise cross-modal understanding and robustness to ambiguous inputs.

Formally, given a medical image $I \in \mathbb{R}^{H \times W \times C}$ and a lesion-focused referring phrase $Q = \{q_1, q_2, \dots, q_n\}$, the task is to generate a binary mask $M \in \{0, 1\}^{H \times W}$ that accurately localizes the lesion referred to by Q . Recent methods fall into two main categories:

Semantic Alignment and Reasoning. These approaches aim to enhance the alignment between clinical language and visual features, often through contrastive learning, causal reasoning, or language-conditioned modeling. Li et al. (Li et al. 2024a) apply multi-level contrastive learning, while CausalCLIPSeg (Chen et al. 2024b) introduces causal interventions to suppress spurious correlations. LViT (Li et al. 2023b) incorporates language-guided attention into transformers for holistic lesion understanding.

Foundation Model Adaptation and Prompt Guidance. This direction focuses on extending the capabilities of pretrained segment models to the medical domain with minimal supervision. LGA (Hu et al. 2024) enables controllable segmentation by injecting language cues into SAM via a lightweight adapter. SimTxtSeg (Xie et al. 2024) and (Huang et al. 2024) utilize prompt-based pseudo-labeling and language-conditioned reconstruction for weakly supervised alignment.

A.4 Unified Medical Reasoning Grounding

Previous tasks have been based on the assumption that clear references to segmented objects are available, which is often challenging in real-world scenarios. Even methods that allow for free-form language descriptions still require unambiguous prompts. In contrast, UMRG starts from a vague reference to anatomical structures and ultimately generates pixel-level segmentation results. This approach alleviates the burden of annotation in the overall workflow and aligns with real-world contexts. In terms of methodology, prior tasks that involve reasoning focused on clarifying the segmentation objects, often decoupling them from the actual

images. Our task, for the first time, associates reasoning with grounding, emphasizing the image cues and a CoT aimed at grounding. The process can be formulated as follows:

Given a medical image \mathcal{I} and a clinical query Q containing implicit referring expressions, the model \mathbf{G} outputs a bounding box \mathcal{B} , two semantic key points \mathcal{P}_1 and \mathcal{P}_2 , and a pixel-level segmentation mask \mathcal{M} . The Task is:

$$\{\mathcal{T}, \mathcal{B}, \mathcal{P}_1, \mathcal{P}_2, \mathcal{M}\} = \mathbf{G}(\mathcal{I}, Q). \quad (11)$$

B More Details on U-MRG-14K Dataset

B.1 Meta Information of U-MRG-14K

Following the established methodologies for constructing diverse datasets (Qiao et al. 2025; Song et al. 2024; Diao et al. 2025a,b; Wang et al. 2025a,b), we design and curate U-MRG-14K with a focus on medical image reasoning across multiple modalities and hierarchical categories.

Comprehensive Image Annotations. To support the generation of faithful and context-aware QA data, we construct enriched meta information for each image. Specifically, we manually annotate each image with key attributes, including **imaging modality**, **subject type** (patient or healthy individual), the **category of the localized structure** (organ or anatomical region), and its broader **super-category** (e.g., *body system* or *scan region*). This meta information ensures consistency across diverse sources and helps establish a structured understanding of the image content. Building on these annotations, we use GPT-4o to generate detailed descriptions using a three-component prompting strategy: **task definition**, **information injection**, and **task refinement**.

Prompt Construction. In the task definition part, we specify the system role and generation principles to constrain the model toward producing accurate and distinctive descriptions. The prompts are iteratively refined to avoid common pitfalls such as diagnostic suggestions or overly generic outputs. For the information injection part, the annotated attributes are translated into natural language with explicit explanations to enhance the model’s comprehension. To precisely anchor the described region, we also provide the model with the actual **segmentation mask**, its **bounding box**, the point **farthest from the mask boundary**, and the point **relatively farthest from it**. To support object-specific adaptation, we categorize the target regions as normal structures, lesions, or ambiguous objects, prompting the model to construct the description from appropriate perspectives—for instance, emphasizing *physiological function* for normal structures, *clinical impact* for lesions, and *strict visual fidelity* for ambiguous regions while explicitly avoiding unwarranted assumptions.

Description Generation. Using these carefully constructed prompts, we generate two complementary descriptions per image–mask pair: (i) a **short description** focused on intuitive visual features (e.g., *shape*, *texture*, *absolute and relative location*), while avoiding medical terminology; and (ii) a **long description** that integrates both medical and imaging knowledge, emphasizing the distinctiveness of the region within its category and in contrast to surrounding

structures. Notably, we observe that for long descriptions, the model tends to default to general medical knowledge rather than precise, image-grounded observations. To address this, we require that **at least half** of the content in the long description be directly grounded in observable visual features. This generation strategy is specifically designed to bridge the gap observed in the Unified Medical Reasoning Grounding (**UMRG**) task, where models often struggle to connect textual interpretations with concrete visual evidence, particularly in clinically nuanced or ambiguous cases. To ensure the quality and reliability of the generated descriptions, all outputs undergo a manual review process, focusing on accuracy, visual relevance, and clinical plausibility. Although we use these descriptions to generate QA data, in the UMRG task, models still struggle to understand and utilize this information directly from the image. Nevertheless, we believe these detailed annotations can serve as a stepping stone toward building a general framework for reasoning grounding in medical images. The example of final generated *meta information* is illustrated in Appendix F.1.

B.2 QA Formats of U-MRG-14K

Context-Aware Prompt Conditioning. For each super-category, we design a short **category scope** prompt to set the GPT-4o’s clinical focus before QA generation. If the super-category is pathological (e.g., *neoplasm*, *infection*), the prompt guides the model to reason about abnormal findings such as tissue changes, lesion extent, and diagnostic uncertainty. If the super-category is anatomical (e.g., *Lung*, *Abdomen*), it shifts focus to normal structure, spatial relations, and physiological function, while discouraging disease assumptions. A short list of fine-grained subclasses (e.g., *left lung*, *right kidney*) is provided for context, but GPT-4o is instructed not to repeat these terms. This conditioning ensures that all questions follow the intended clinical perspective and remain deliberately vague.

Schema-Guided QA-Format Generation. After setting the clinical scope, we present GPT-4o with one structured prompt that requests exactly N question–answer formats (default $N = 20$). The prompt explains that each question should resemble a vague inquiry from a patient, pointing to the target only through visual or functional clues while avoiding technical labels. Each answer is limited to five sentences and must describe a clear, step by step visual reasoning path without offering a diagnosis. To ensure variety, the instructions demand that wording, cue type, and reasoning style differ across formats. Finally, the model must return its output as a strict JSON object that contains the super-category name and a list of $\{id, question, answer\}$. Because this schema is embedded in the prompt, the result is immediately machine-verifiable and ready for downstream use. Combined with the context-aware prompt, this procedure yields QA formats that are clinically sound, broadly applicable within each super-category, and fully consistent with the UMRG evaluation protocol. The example of final generated *QA formats* is illustrated in Appendix F.2.

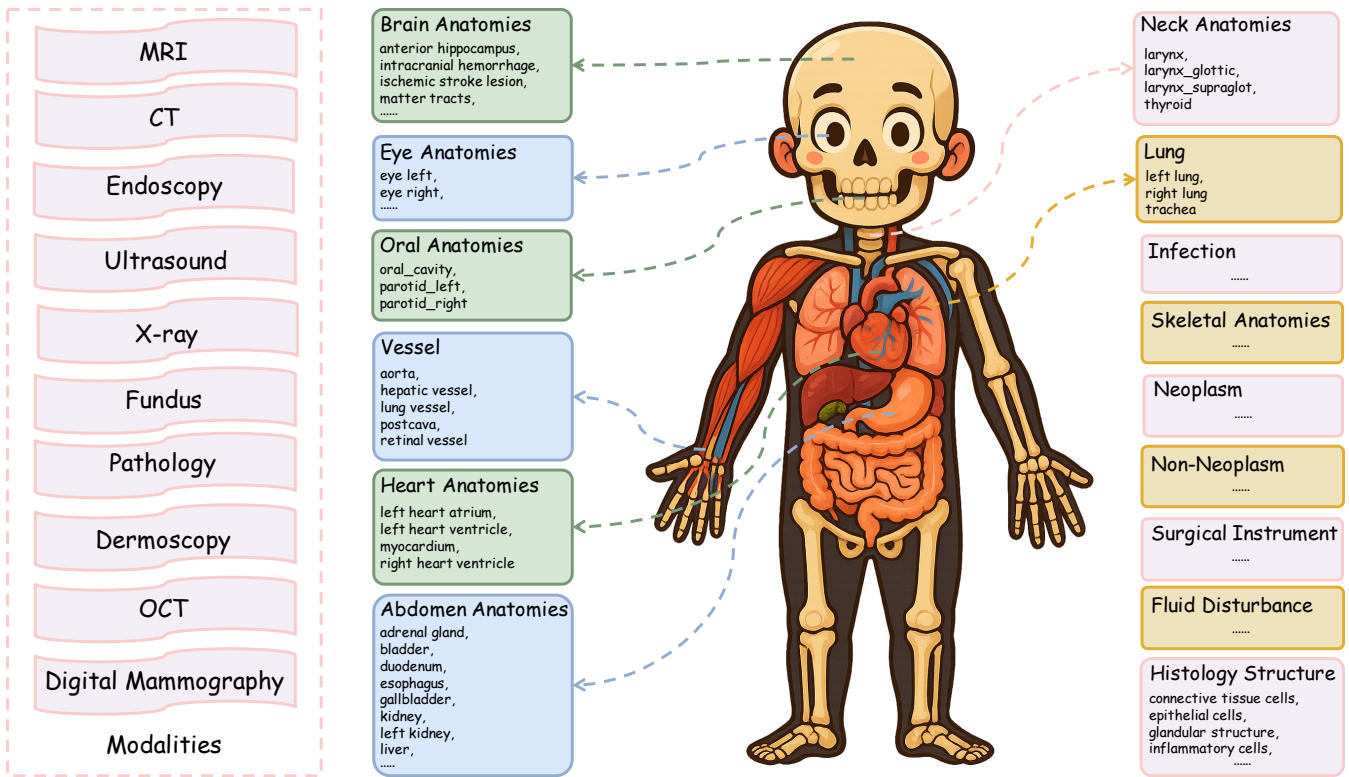


Figure 5: Overview of Modalities and Hierarchical Category Structure in the U-MRG-14k Dataset.

B.3 QA Pairs of U-MRG-14K

QA Pair Design for the UMRG Task. The QA pair data is designed to serve the **Unified Medical Reasoning Grounding (UMRG) task**, which is closely aligned with real-world scenarios. The detailed reasoning data included also provides room for future expansion in subsequent SFT work. To achieve this, we designed a specific format for our question-answering pairs that differs significantly from traditional VQA datasets. Our deliberately **ambiguous questions** are crafted to train the model’s foundational visual reasoning and localization capabilities, rather than simple object recognition. Critically, the corresponding answers are designed as explicit Chain-of-Thought (**CoT**) reasoning pathways. The intention is that these detailed logical inferences are particularly beneficial for bootstrapping a model’s reasoning abilities from a cold start.

A Multi-part Prompting Framework. To generate QA pairs that meet the above design, we developed a detailed, multi-part Prompting Framework that guides the model through a sequence of understanding, reasoning, and generation; such a structured approach is essential for managing the complexity of clinical reasoning. This framework is composed of three core components delivered in a single, cohesive prompt. First, it **assigns the model the role** of a professional radiologist; this initial instruction primes the model to activate its domain-specific knowledge and adopt a professional, analytical tone, rather than a conversational one. Second, it grounds the model in facts by injecting a rich, multi-

modal context. This includes the medical image, a segmentation mask, and extensive metadata such as *imaging modality*, *patient health status*, *anatomical classifications (super-category, category)*, *precise spatial coordinates (bbox, key points)*, and *textual descriptions*. Providing this comprehensive evidence base is vital to minimize hallucination, a common failure mode for LLMs, and ensures all reasoning is anchored in verifiable data. Third, it defines the core task: the model must **revise a given QA template** to align with the provided image content. This revision process is governed by a strict set of rules designed to elicit deep reasoning. The question must be revised to be vague and indirect, grounded in the region’s visual attributes without revealing the category name, which forces the model to engage in genuine visual search rather than simple keyword matching. The answer must follow a **step-by-step logical path** based solely on observable visual features, remain non-diagnostic, and clearly identify the true category, making its reasoning process transparent and auditable. To enforce this deep visual reasoning, the most notable principle is the **“Pretend the Mask is Unavailable” Principle**. This instruction is critical as it compels the model to mimic human expert cognition—analyzing the broader anatomical context to progressively narrow down and localize the specific finding, rather than taking a shortcut by simply referring to the mask’s coordinates. This entire strategy culminates in a structured JSON output, which facilitates reliable downstream processing and automated evaluation of the generated dataset. The example

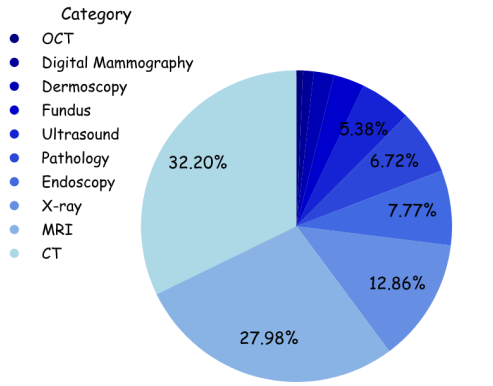


Figure 6: Pie chart illustrating the distribution of imaging modalities in the whole U-MRG-14K dataset.

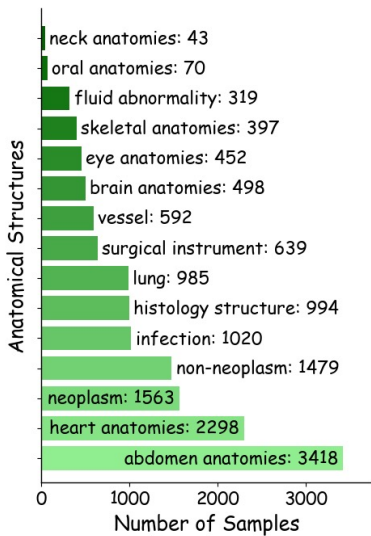


Figure 7: Bar chart illustrating the distribution of super-categories in the whole U-MRG-14K dataset.

of final generated QA pairs is illustrated in Appendix F.3.

B.4 Dataset Statistics

U-MRG-14K is, to our knowledge, the first dataset that combines implicit clinical questions with pixel annotations (*bounding boxes*, *interior key points*, and *masks*), across a wide range of imaging studies. It spans **10 medical modalities** (CT, MRI, ultrasound, histology, etc.), **15 super-categories**, and **108 fine-grained categories**. A summary of the overall distribution is shown in Fig. 5. The specific proportions of these imaging modalities and super-categories are illustrated in Fig. 6 and Fig. 7.

Detailed Distribution. The four largest super-categories in the dataset, namely *abdomen*, *heart*, *neoplasm*, and *non-neoplasm*, collectively account for **59 %** of all samples. This highlights the dataset’s alignment with the predomi-

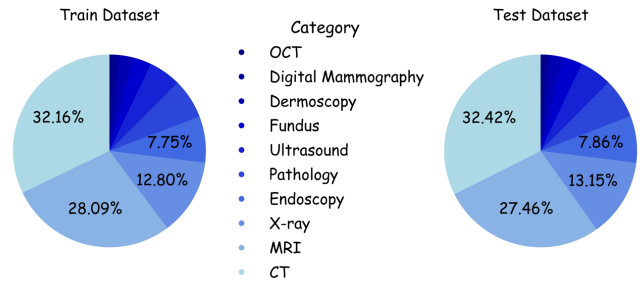


Figure 8: Pie chart illustrating the distribution of imaging modalities in the U-MRG-14K dataset. The **left** panel shows the percentage of samples per modality in the training set, while the **right** panel shows the corresponding distribution in the test set.

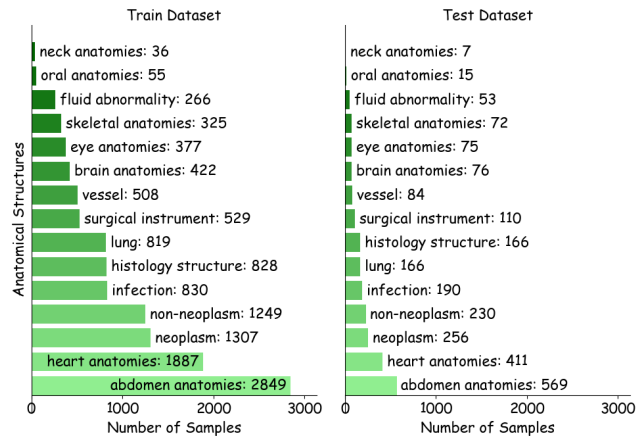


Figure 9: Bar chart illustrating the distribution of super-categories in the U-MRG-14K dataset. The **left** panel shows the number of samples per super-category in the training set, while the **right** panel shows the corresponding distribution in the test set.

nant trends in current open-source medical datasets. We partition U-MRG-14K into distinct training and testing splits to support systematic evaluation. The distribution of imaging modalities within each split is shown in Fig. 8, and the super-category composition is illustrated in Fig. 9.

Future Extension. We are actively expanding the underlying collection pipeline and will release updated versions that broaden modality and category coverage, ultimately providing a more comprehensive resource to support the development and evaluation of solutions for the UMRG task.

C More Details on MedReasoner Framework

C.1 Group Relative Policy Optimization.

We utilize Group Relative Policy Optimization (GRPO) (Shao et al. 2024) as our reinforcement learning strategy. It is an efficient reinforcement learning algorithm that eliminates the need for a value network by leveraging group-wise relative advantages. For each input query q , GRPO samples a

group of G outputs $\{o_i\}_{i=1}^G$ from the old policy π_{old} , scores them using a reward model r_ϕ , and computes normalized relative advantages within the group. The policy π_θ is updated by maximizing the following objective:

$$J_{\text{GRPO}}(\theta) = \mathbb{E}_{q, \{o_i\}_{i=1}^G \sim \pi_{\text{old}}} \left[\frac{1}{G} \sum_{i=1}^G \frac{1}{|o_i|} \sum_{t=1}^{|o_i|} \left(\min \left(\frac{\pi_\theta(o_{i,t} | q, o_{i,<t})}{\pi_{\text{old}}(o_{i,t} | q, o_{i,<t})} \hat{A}_{i,t}, \right. \right. \right. \\ \left. \left. \left. \text{clip} \left(\frac{\pi_\theta(o_{i,t} | q, o_{i,<t})}{\pi_{\text{old}}(o_{i,t} | q, o_{i,<t})}, 1-\epsilon, 1+\epsilon \right) \hat{A}_{i,t} \right) - \beta D_{\text{KL}}[\pi_\theta \parallel \pi_{\text{ref}}] \right) \right] \quad (12)$$

where $r_{i,t} = \frac{\pi_\theta(o_{i,t} | q, o_{i,<t})}{\pi_{\text{old}}(o_{i,t} | q, o_{i,<t})}$ is the token-level importance ratio, and $\hat{A}_{i,t}$ denotes the normalized advantage computed via one of the following supervision strategies:

Outcome Supervision. A single scalar reward r_i is assigned to each sampled output o_i by the reward model. The group-wise normalized reward is computed as:

$$\hat{A}_{i,t} = \tilde{r}_i = \frac{r_i - \mu_r}{\sigma_r}, \quad \forall t, \quad (13)$$

where μ_r and σ_r denote the mean and standard deviation of $\{r_1, \dots, r_G\}$.

Process Supervision. Step-level rewards $r_i^{(j)}$ are assigned to each intermediate reasoning step based on its contribution, and the advantage is computed accordingly as:

$$\hat{A}_{i,t} = \sum_{j: \text{index}(j) \geq t} \tilde{r}_i^{(j)}, \quad \text{where } \tilde{r}_i^{(j)} = \frac{r_i^{(j)} - \mu_R}{\sigma_R}. \quad (14)$$

GRPO aligns well with the relative nature of reward models trained on pairwise preference data, and it significantly reduces the computational burden by avoiding the training of a separate value network.

C.2 User Prompts

Reasoning User Prompt. The design of these prompts is guided by principles that ensure precise, clinically grounded visual grounding within a tightly defined output format. The prompt **explicitly defines the task** as localizing anatomical or pathological regions across diverse medical imaging modalities, and makes clear to the model that natural language questions may lack explicit spatial references—requiring inference based on clinical context and visual cues. To address this, the prompt enforces a **structured reasoning process** resembling clinical diagnostic logic: generating a hypothesis based on medical context, systematically inspecting visual features, and iteratively refining the inference. This process culminates in visual grounding, achieved by aligning domain knowledge with observable cues such as shape, density, texture, and structural variation. The **required output** consists of a `think` block articulating

unambiguous clinical reasoning, followed by an `answer` block containing a precise bounding box and two interior key points. This design promotes accuracy, reproducibility, and interpretability, while explicitly restricting diagnostic speculation and minimizing ambiguity in localization. In all experiments presented in this work, any response explicitly labeled as *reason* was generated using this prompt.

Direct User Prompt. This prompt specifies a direct localization task in medical images, requiring spatial outputs **without an explicit reasoning trace**. The model receives a natural language question and must respond solely with an `answer` block containing a structured json object: a tight bounding box enclosing the target region and two distinct key points. Unlike reasoning-based prompts, this version provides no guidance on interpreting ambiguous queries or incorporating clinical context. Any response explicitly labeled as *without reason* was generated using this prompt.

C.3 Reward Functions

BBox IoU Reward. The **IoU reward** quantifies the spatial overlap between a predicted bounding box \mathcal{B}_p and a ground truth bounding box \mathcal{B}_g . It is defined as the ratio of their intersection area to their union area:

$$\mathbb{R}_{\text{iou}} = \frac{\text{Area}(\mathcal{B}_p \cap \mathcal{B}_g)}{\text{Area}(\mathcal{B}_p \cup \mathcal{B}_g)}. \quad (15)$$

This metric ranges from 0 (no overlap) to 1 (perfect overlap), with higher values indicating better localization accuracy.

BBox Alignment Reward. The **Alignment reward** measures the average L1 distance between corresponding corner coordinates of the predicted bounding box \mathcal{B}_p and the ground truth bounding box \mathcal{B}_g . This distance is then normalized by the diagonal length of \mathcal{B}_g to ensure scale invariance. Formally, it's expressed as:

$$\mathbb{R}_{\text{align}} = \frac{1}{4} \sum_{i=1}^4 \left| \mathcal{B}_p^{(i)} - \mathcal{B}_g^{(i)} \right|. \quad (16)$$

A lower $\mathbb{R}_{\text{align}}$ value signifies superior positional alignment, making it a direct indicator of how closely the predicted box's corners match those of the ground truth.

BBox Scale Reward. The **Scale reward** measures structural consistency between a predicted box and its ground truth, considering both area and aspect ratio. It computes the Euclidean distance between the logarithmic differences of the box areas and aspect ratios:

$$\mathbb{R}_{\text{scale}} = \sqrt{(\Delta \log A)^2 + (\Delta \log R)^2}, \quad (17)$$

where $\Delta \log A$ and $\Delta \log R$ denote the logarithmic differences in box area and aspect ratio, respectively. A smaller $\mathbb{R}_{\text{scale}}$ value indicates superior structural alignment, reflecting a better match in shape and proportionality.

Points Dice (pDice) Reward. The **Points Dice (pDice) reward** evaluates the spatial correspondence between a predicted keypoint pair $\mathcal{P}_p = \{\mathbf{p}_1^p, \mathbf{p}_2^p\}$ and a ground-truth keypoint pair $\mathcal{P}_g = \{\mathbf{p}_1^g, \mathbf{p}_2^g\}$. This reward models each point

User Prompt for U-MRG (w/ Reasoning)

```

"<image>"
"This is a medical image localization task. Modalities include X-ray, CT, MRI, ultrasound, endoscopy, fundus, pathology, dermoscopy, and mammography."
"The question provides only implicit cues about the target region. Begin by inferring its likely focus as a clinician would."
"Your goal is to use rigorous visual reasoning to identify the anatomical or pathological region implied by the question and precisely locate it in the image."
"Think step by step to answer the question and accurately ground the target in the image."
"Question: {Question}"
"Step-by-step guidelines:"
"1. Interpreting the vague question: The question may not explicitly describe the target. Start by hypothesizing its implied intent using prior clinical knowledge and general context."
"2. Gathering visual evidence: Systematically inspect the image and extract relevant visual features—such as shape, edge definition, brightness or density, symmetry, texture, and structural heterogeneity—to validate or revise your initial hypothesis."
"3. Inferring the most likely target region: Integrate your clinical hypothesis with visual observations. Narrow down to a single region that best matches the implied intent of the question, guided by the most salient visual cues."
"4. Delivering precise localization: Express your conclusion by providing only spatial location details (bounding box and points). Omit diagnosis or classification."
"5. Resolving inconsistencies: If earlier reasoning conflicts with visible evidence, revise your interpretation and prioritize the observed visual data."
"Output Formats:"
"Your response must adhere to a strict format, containing exactly one <think> block followed immediately by one <answer> block:"
"- <think>...</think>: Use clinical reasoning to precisely explain how the observed visual features and relevant medical context were integrated to determine the target region in the image."
"- <answer>...</answer>: This section must contain a JSON object with the following keys and values:"
"  \ "bbox\ ": the tightest bounding box enclosing the target region."
"  \ "points_1\ ": a primary key point within the bbox, on the target region."
"  \ "points_2\ ": a second, distinct key point within the target region."
"Response Rules:"
"- The entire output must be a single continuous string, containing precisely one <think> block and one <answer> block, with no additional text or formatting."
"- The <think> section must exclusively reflect confident clinical reasoning focused on precise localization, without any hedging, ambiguity, or expressions of uncertainty."
"- The <answer> block must not be empty. You must always output a valid bounding box and two key points."
"- The bounding box must be the tightest possible rectangle that completely encloses the target region, excluding any background pixels."
"- The two key points must have distinct coordinates, lie strictly within the target region, and correspond to different salient visual cues."
"Example Output:"
"<think> thinking process here </think>"
"<answer>{ 'bbox': [xmin, ymin, xmax, ymax], 'points_1': [x1, y1], 'points_2': [x2, y2]}</answer>"

```

Figure 10: **Reasoning User Prompt.** Prompt variant used in RL training and *with-reasoning* evaluation. The model must (1) generate a `<think>` block that walks through step-by-step visual reasoning, then (2) output an `<answer>` block containing a JSON object with a tight bounding box and two interior key points.

pair as the diameter of a circle, O_p and O_g respectively. The Dice score is then computed to quantify the spatial overlap between these circles:

$$\mathbb{R}_{\text{pdice}} = \frac{2 \cdot \text{Area}(O_p \cap O_g)}{\text{Area}(O_p) + \text{Area}(O_g)}. \quad (18)$$

A higher $\mathbb{R}_{\text{pdice}}$ value indicates better spatial alignment and consistency between the regions defined by the predicted and ground-truth keypoint pairs.

Points Alignment Reward. The **Alignment reward** quantifies the positional accuracy of predicted keypoints by computing the mean absolute error between corresponding points in a predicted pair $\mathcal{P}_p = \{\mathbf{p}_1^p, \mathbf{p}_2^p\}$ and a ground truth pair $\mathcal{P}_g = \{\mathbf{p}_1^g, \mathbf{p}_2^g\}$. It is formulated as:

$$\mathbb{R}_{\text{align}} = \frac{1}{2} \sum_{i=1}^2 (|x_i^p - x_i^g| + |y_i^p - y_i^g|). \quad (19)$$

A lower $\mathbb{R}_{\text{align}}$ value signifies superior positional alignment, indicating that the predicted keypoints are precisely located

relative to their ground truth counterparts.

Points Angle Reward. The **Angle reward** quantifies the angular consistency between a predicted keypoint pair and its ground-truth counterpart. It computes the absolute cosine similarity between their respective direction vectors, $\mathbf{v}_p = \mathbf{p}_2^p - \mathbf{p}_1^p$ and $\mathbf{v}_g = \mathbf{p}_2^g - \mathbf{p}_1^g$:

$$\mathbb{R}_{\text{angle}} = |\cos(\theta)| = \left| \frac{\langle \mathbf{v}_p, \mathbf{v}_g \rangle}{\|\mathbf{v}_p\|_2 \cdot \|\mathbf{v}_g\|_2} \right|, \quad (20)$$

where θ is the angle between the vectors. A higher $\mathbb{R}_{\text{angle}}$ value (closer to 1) indicates superior angular alignment, signifying that the orientation defined by the predicted points closely matches that of the ground-truth.

C.4 Smoothing and Penalization

Smoothing. To enhance training stability and provide a more nuanced differentiation of prediction quality, all reward components are processed by dedicated smoothing

User Prompt for U-MRG (w/o Reasoning)

```

"<image>"
"Please answer {Question} with bbox and points."
"Output Formats:"
"Your response must adhere to a strict format, containing exactly one <answer> block:"
"- <answer> ... </answer>: This section must contain a JSON object with the following keys and values:"
"  \"bbox\": the tightest bounding box enclosing the target region."
"  \"points_1\": a primary key point within the bbox, on the target region."
"  \"points_2\": a second, distinct key point within the target region."
"Example Output: "
"<answer>{\"bbox\": [xmin, ymin, xmax, ymax], \"points_1\": [x1, y1], \"points_2\": [x2, y2]}</answer>"

```

Figure 11: **Direct User Prompt.** Prompt variant for the *without-reasoning* baseline. The model skips the explicit reasoning trace and returns only the `<answer>` block with a JSON object with a tight bounding box and two interior key points.

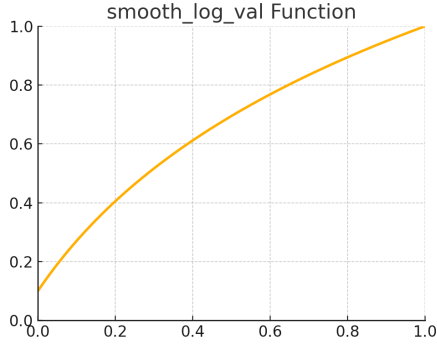


Figure 12: Visualization of the logarithmic smoothing function, showing the smoothing reward growth from 0.1 to 1.0 over the input range $[0, 1]$.

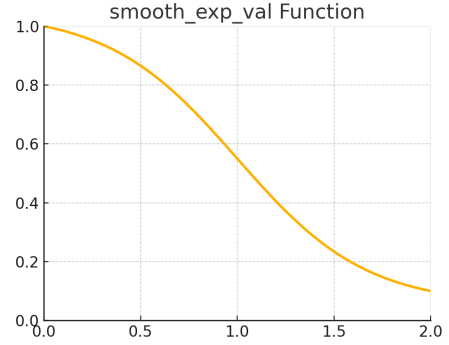


Figure 13: Visualization of the exponential smoothing function, illustrating a smooth exponential decay from 1.0 to 0.1 over the input range $[0, 2]$, centered around $x = 1.0$.

functions. These transformations convert raw reward values or distances into a smoothed range, making them more suitable for reinforcement learning optimization.

For rewards where a higher value indicates better performance (e.g., \mathbb{R}_{iou} , $\mathbb{R}_{\text{pdice}}$, and $\mathbb{R}_{\text{angle}}$), **logarithmic smoothing** is applied. This function, given by:

$$\mathcal{S}_{\log}(r; k) = \frac{\log(kr + 1)}{\log(k + 1)}, \quad (21)$$

maps the raw reward $r \in [0, 1]$ to a smoothed value. The parameter k (default $k = 3$) acts as a **scaling factor**, controlling the curvature of the logarithmic function. This smoothing compresses higher reward values while expanding the differences among lower reward values, providing stronger gradients for initial improvements when the raw reward is small. This behavior is illustrated in Fig. 12.

For rewards where a lower value indicates better performance (e.g., $\mathbb{R}_{\text{align}}$ and $\mathbb{R}_{\text{scale}}$), **exponential smoothing** is utilized. This function, defined as:

$$\mathcal{S}_{\exp}(d; k, c) = \frac{1}{1 + e^{k(d-c)}}, \quad (22)$$

transforms the normalized distance $d \in [0, 2]$ into a smoothed reward. Here, k (default $k = 3$) controls the **steepness** of the sigmoid-like curve, and c (default $c = 1$) represents the **target center**, shifting the inflection point of

the curve. This smoothing assigns higher rewards when the distance d is small and rapidly decreases the reward as d increases, effectively penalizing larger deviations more aggressively. This behavior is visualized in Fig. 13.

Penalization. After applying smoothing functions, we further refine the reward signal through a penalization function $\mathcal{N}(\cdot)$. The primary purpose of this penalization is to softly down-weight unreliable predictions, ensuring that the learning agent is not overly rewarded for outputs that are spatially implausible or inconsistent. For each smoothed reward, two validity scores, v_1 and v_2 , are computed. These scores are designed to reflect the spatial plausibility of the predicted output based on different criteria.

For **BBox-based rewards** (\mathbb{R}_{iou} , $\mathbb{R}_{\text{align}}$, $\mathbb{R}_{\text{scale}}$): (1) One validity score checks if the ground truth points are largely contained within the predicted bounding box. This ensures the predicted box correctly encloses the target. (2) Another score assesses the plausibility of the predicted bounding box's area relative to the ground truth. For instance, if a predicted box is excessively large or small compared to the ground truth, it would receive a lower validity score.

For **Points-based rewards** ($\mathbb{R}_{\text{pdice}}$, $\mathbb{R}_{\text{align}}$, $\mathbb{R}_{\text{angle}}$): (1) One validity score ensures the predicted keypoints are within a plausible spatial range, such as within the ground truth box or image boundaries. (2) Another score evaluates the spatial

spread or separation of the predicted keypoints. If the points are too close together (e.g., collapsing to a single point) or too far apart, it suggests an unreliable prediction.

The final reward is adjusted using the following formula:

$$\mathcal{N}(r; v_1, v_2) = \lambda r + (1 - \lambda)r \cdot \frac{v_1 + v_2}{2}, \quad (23)$$

where r is the smoothed reward, v_1 and v_2 are the two validity scores (typically ranging from 0 to 1, with 1 indicating high validity and 0.5 indicating moderate validity in the provided context), and λ is a mixing coefficient (default $\lambda = 0.7$). This formula linearly combines the smoothed reward with a weighted average of the smoothed reward scaled by the validity scores. The parameter λ controls the influence of the raw smoothed reward versus the validity-adjusted reward. A higher λ places more emphasis on the smoothed reward, while a lower λ allows the validity scores to more significantly penalize unreliable predictions. This penalization mechanism acts as a soft constraint, discouraging the model from making outputs that, despite potentially having a reasonable IoU or alignment, are fundamentally illogical in their spatial configuration.

D More Details on Experiments

D.1 Implementation Details

We adopt Lingshu-7B (Xu et al. 2025) and MedSAM2 (Ma et al. 2025) as our default CRM and ASM, respectively. MedReasoner is trained on an 8 NVIDIA A100-80G GPUs with the veRL (Sheng et al. 2025). Training utilized a total batch size of 5 and 16 samples per step. The initial learning rate is set to $1e-6$. In terms of generation configuration, we follow the same settings as used in Lingshu, setting the repetition penalty to 1.05 and the temperature to 0.1, while employing argmax sampling.

D.2 Model Details

GPT-4o (OpenAI 2024) GPT-4o is a multimodal, decoder-only closed-source language model capable of processing text, vision, and audio within a unified architecture. It is trained end-to-end on mixed-modality data and optimized for reasoning, instruction following, and real-time interaction. GPT-4o achieves strong performance across many standard academic benchmarks.

Gemini 2.5 Flash (Google 2025) Gemini 2.5 Flash is a lightweight text-to-text decoder model derived from Google’s Gemini series, optimized for efficiency and low-latency applications. Despite its compact design, it supports multimodal inputs (text, code, image, audio, video) and features a 1M-token context window. The model excels in reasoning and language understanding benchmarks.

Qwen2.5-VL (Bai et al. 2025) Qwen2.5-VL extends the Qwen2.5 language model with advanced multimodal capabilities, integrating a vision encoder enhanced by dynamic resolution training, window attention, SwiGLU, and RMSNorm. It achieves robust visual reasoning performance across charts, texts, and layouts.

InternVL3 (Chen et al. 2024d) InternVL3 is a multi-modal decoder-based model built upon a Qwen2.5-derived language backbone and a newly pre-trained vision encoder, following the ViT-MLP-LLM architecture. It adopts Native Multimodal Pre-Training on text, image, and video data, enabling strong long-context understanding and tool-use reasoning across domains such as 3D vision and GUI agents.

Med-R1 (Lai et al. 2025) Med-R1 is a reinforcement learning-enhanced vision-language model tailored for medical tasks across eight imaging modalities. It employs Group Relative Policy Optimization (GRPO) to improve generalization in tasks such as disease diagnosis and lesion grading, surpassing Qwen2-VL-72B by a significant margin.

MiniInternVL (Gao et al. 2024) MiniInternVL, part of InternVL2.0, is a compact multimodal instruction-tuned model built with InternViT-300M, an MLP projector, and Phi-3-mini-128k. It supports high-resolution images and long-video inputs, demonstrating efficient performance in diverse vision-language tasks.

MedGemma (Sjellergren et al. 2025) MedGemma is based on Gemma 3 and integrates a MedSigLLIP encoder pre-trained on de-identified medical images, with language components trained on medical text. Optimized for instruction tuning, the model supports medical applications such as report summarization and diagnosis explanation.

HuatuoGPT (Chen et al. 2024a) HuatuoGPT is a Chinese medical instruction-tuned LLM based on LLaMA, designed for diagnostic consultations. It is fine-tuned using synthetic instructions from ChatGPT and real doctor-patient dialogues. The model demonstrates strong performance in symptom interpretation and treatment recommendation.

Lingshu (Xu et al. 2025) Lingshu is a medical MLLM built on Qwen2.5-VL, integrating a vision encoder, LLM, and projection module. Trained via a multi-stage process with RL using verifiable rewards, it leverages over 5 million multimodal and textual medical samples. It supports unified understanding across multiple imaging types

Chiron-o1 (Sun et al. 2025) Chiron-o1 is an MLLM fine-tuned from InternVL using a collaborative search architecture involving mentor-trainee feedback loops to enhance reasoning. It excels in benchmark reasoning tasks by generating interpretable reasoning paths.

MedSAM (Ma et al. 2024) Built upon the Segment Anything Model (SAM), MedSAM is fine-tuned on a large-scale dataset of 1.57 million image-mask pairs, spanning 10 medical imaging modalities and over 30 cancer types. MedSAM adopts a promptable segmentation approach using bounding boxes to flexibly specify regions of interest, which enables clinicians to guide segmentation according to varied needs.

SAM-Med2D (Cheng et al. 2023) SAM-Med2D bridges this domain gap by fine-tuning SAM on a large-scale medical image dataset comprising approximately 4.6 million images and 19.7 million masks. Unlike earlier adaptations which focused on limited prompt types or small datasets, SAM-Med2D supports a full spectrum of prompts—points,

bounding boxes, and masks—enabling robust interactive segmentation across complex clinical scenarios.

MedSAM2 (Ma et al. 2025) MedSAM2 is a generalized auto-tracking model designed for universal 2D and 3D medical image segmentation. Built upon SAM2, MedSAM2 treats medical image segmentation as a video object tracking task to unify the processing of unordered 2D slices and volumetric 3D scans. A key innovation is its self-sorting memory bank, which dynamically selects and resamples embeddings.

SAM4MLLM (Chen et al. 2024c) SAM4MLLM integrates the Segment Anything Model (SAM) with MLLMs to perform Referring Expression Segmentation using a purely text-based training objective. It introduces Prompt-Point Generation and Proactive Query mechanisms to generate and refine segmentation prompts. Notably, the model retains the original MLLM architecture, enabling pixel-level localization without structural changes.

VLM-R1 (Shen et al. 2025) VLM-R1 adapts rule-based reinforcement learning from DeepSeek-R1 for vision tasks like REC and OVD, using a novel odLength metric to avoid reward hacking. Built on Qwen2.5VL-3B, it enables complex visual reasoning behaviors such as emergent "aha" moments. The framework enhances generalizability via task-specific visual feedback signals.

SegZero (Liu et al. 2025) SegZero combines Qwen2.5-VL and SAM2 within a reinforcement learning framework for zero-shot reasoning segmentation. It decouples reasoning and segmentation by using CoT prompts and a frozen segmentation module. Trained without annotated reasoning data, it achieves SOTA results on ReasonSeg.

D.3 Out-of-Distribution Experiments

To evaluate generalization, we created a biased training set, **U-MRG-6K**, using 6K images from the 5 most frequent categories in U-MRG-14K. The remaining images from the other 9 categories served as the out-of-distribution (OOD) test set. We then trained the CRM on U-MRG-6K using (1) SFT and (2) three RL variants. We evaluated their performance under different prompting strategies.

Table 6 shows that SFT suffers from severe phrase overfitting: without explicit reasoning, it refused 91% of OOD queries, and even with reasoning, its accuracy dropped below the base model. In contrast, all RL variants outperformed the base and SFT models across all metrics, confirming the benefit of reinforcement learning for implicit-query grounding when the test distribution shifts. Furthermore, both RL variants (excluding the base) were robust to prompt variations in OOD situation, maintaining grounding performance even without detailed task instructions, whereas SFT heavily relied on reasoning-path prompts to avoid refusals.

D.4 Qualitative Results

Based on our observations of the output generated by various models, we found that GPT-4o, despite being a closed-source commercial model capable of **producing comprehensive reasoning paths** and generally correct interpreta-

Method	Reason	IoU \uparrow	pDice \uparrow	Dice \uparrow	# Ref. \downarrow
SFT	✗	0.32	0.08	0.55	1081
SFT	✓	6.32	1.56	13.45	0
RL-Base	✗	8.11	1.93	14.72	1
RL-Base	✓	16.09	9.78	24.91	0
RL-Hard	✗	16.08	10.85	23.28	1
RL-Hard	✓	16.92	<u>11.85</u>	24.34	0
RL-Soft	✗	<u>17.27</u>	12.02	<u>25.2</u>	0
RL-Soft	✓	17.67	11.33	26.72	0

Table 6: Performance on the OOD split with Lingshu-7B as the CRM. Models are trained on **U-MRG-6K** (five frequent categories) and tested on unseen classes.

tions of ambiguous questions, fails to translate this understanding into accurate grounding. This shortcoming reveals **a lack of pixel-level comprehension** of medical images, as evidenced by its tendency to produce bounding boxes with coordinates rounded to multiples of 10.

Qwen2.5VL, a powerful open-source general-purpose MLLM, demonstrates better alignment between textual and visual content and is **able to produce relatively precise grounding** results. However, its limited medical knowledge hinders its ability to **infer correct targets from ambiguous queries**, and it lacks domain-specific understanding of uncommon medical imaging modalities such as histopathological slides and fundus images.

Lingshu, a model further trained on medical tasks, is capable of correctly reasoning and identifying targets in ambiguous contexts. Nonetheless, it remains inadequate in **translating natural language-based grounding into bounding boxes or point coordinates** that can be effectively utilized by segmentation models.

In contrast, our model, trained with a GRPO objective that **incorporates a pixel-level grounding reward**, successfully aligns natural language reasoning with pixel-level grounding. It achieves accurate interpretation of ambiguous referents and bridges the gap left by existing models.

E Broaden Impact

E.1 Societal Impact

Our dataset is anticipated to have a significant positive impact on both medical research and clinical practice. By providing a high-quality, publicly available benchmark, it can accelerate the development and validation of novel image segmentation algorithms, thereby **pushing forward the broader scientific research process**. Models trained on this dataset can **effectively assist physicians in diagnosis** by enabling faster and more accurate delineation of pathological regions, which is crucial for treatment planning and disease monitoring. However, it is crucial to acknowledge potential risks. **Over-reliance on AI-driven tools without proper clinical oversight could lead to serious diagnostic errors**. Therefore, we advocate that these models should be used as assistive tools to augment, not replace, clinical expertise. The use of this dataset and any derived models for direct

clinical decision-making without rigorous, independent validation and regulatory approval is strongly discouraged.

E.2 Ethics Statement

We have ensured strict adherence to all applicable ethical guidelines. Our dataset is compiled exclusively from **publicly available datasets where the original providers have explicitly affirmed that patients provided informed consent** for their data to be used in research. All data has been rigorously and consistently anonymized to remove any personal patient information and protect patient privacy before inclusion in our collection. This dataset is intended **solely for academic and non-commercial purposes. Any unauthorized commercial use is strictly prohibited.** We urge all users to respect this provision to maintain the integrity and ethical standing of this valuable resource.

F Case Study

F.1 Meta Information of U-MRG-14K

We illustrate the **meta information** design using 15 representative cases, with one example selected from each super-category and arranged across Fig. 16 to Fig. 30. For each image in the dataset, we construct a set of information that includes several key attributes, such as **imaging modality** and **subject health status**. In addition, we provide a pair of carefully designed textual descriptions for each case: a **short description** that captures key visual cues in plain and intuitive language, and a **long description** that incorporates domain-specific knowledge to emphasize the region’s clinical relevance and distinctiveness.

F.2 QA Formats of U-MRG-14K

We illustrate the **QA formats** design using 15 representative cases, with two examples selected from each super-category and arranged across Fig. 21 to Fig. 25. Each case includes a concise explanation of the corresponding super-category and showcases two representative QA formats that capture diverse *query intents* and *reasoning strategies*. The formats cover common clinical scenarios such as *location reference*, *attribute reasoning*, and *structural inference*, reflecting how our prompt design accommodates linguistic ambiguity while aligning with medical grounding objectives.

F.3 QA Pairs of U-MRG-14K

We illustrate the **QA pairs** design using 15 representative cases, with one example selected from each super-category and arranged across Fig. 26 to Fig. 30. For each image in the dataset, we construct a set of information that includes several key attributes, such as **imaging modality** and **subject health status**. In addition, we provide a set of carefully constructed QA pairs for each case. The **question** is formulated with implicit clinical reasoning and manually filtered to align with the UMRG task requirements. The **think** field captures a step-by-step reasoning path generated by GPT-4o, simulating a clinician’s thought process and enabling analysis of the model’s understanding. The **answer** contains accurate spatial grounding derived from the annotated mask, including a bounding box and two key points.

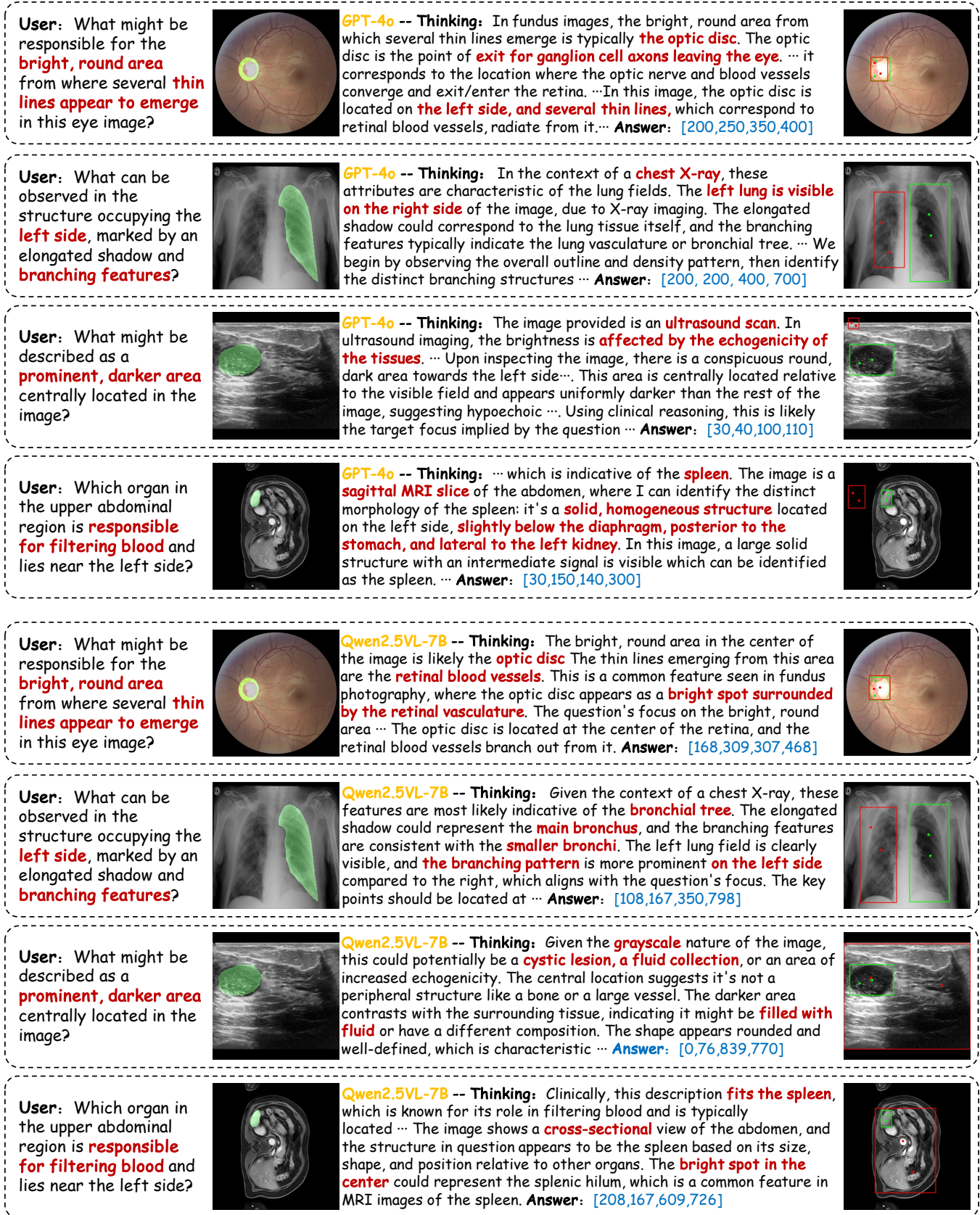


Figure 14: The top four rows show GPT-4o's responses in different cases, while the bottom four rows present those of Qwen2.5VL-7B. For each case, the columns from left to right represent the ambiguous query, the image input with the ground-truth mask, the model's reasoning process, and the model's output including the predicted bounding box and keypoints.

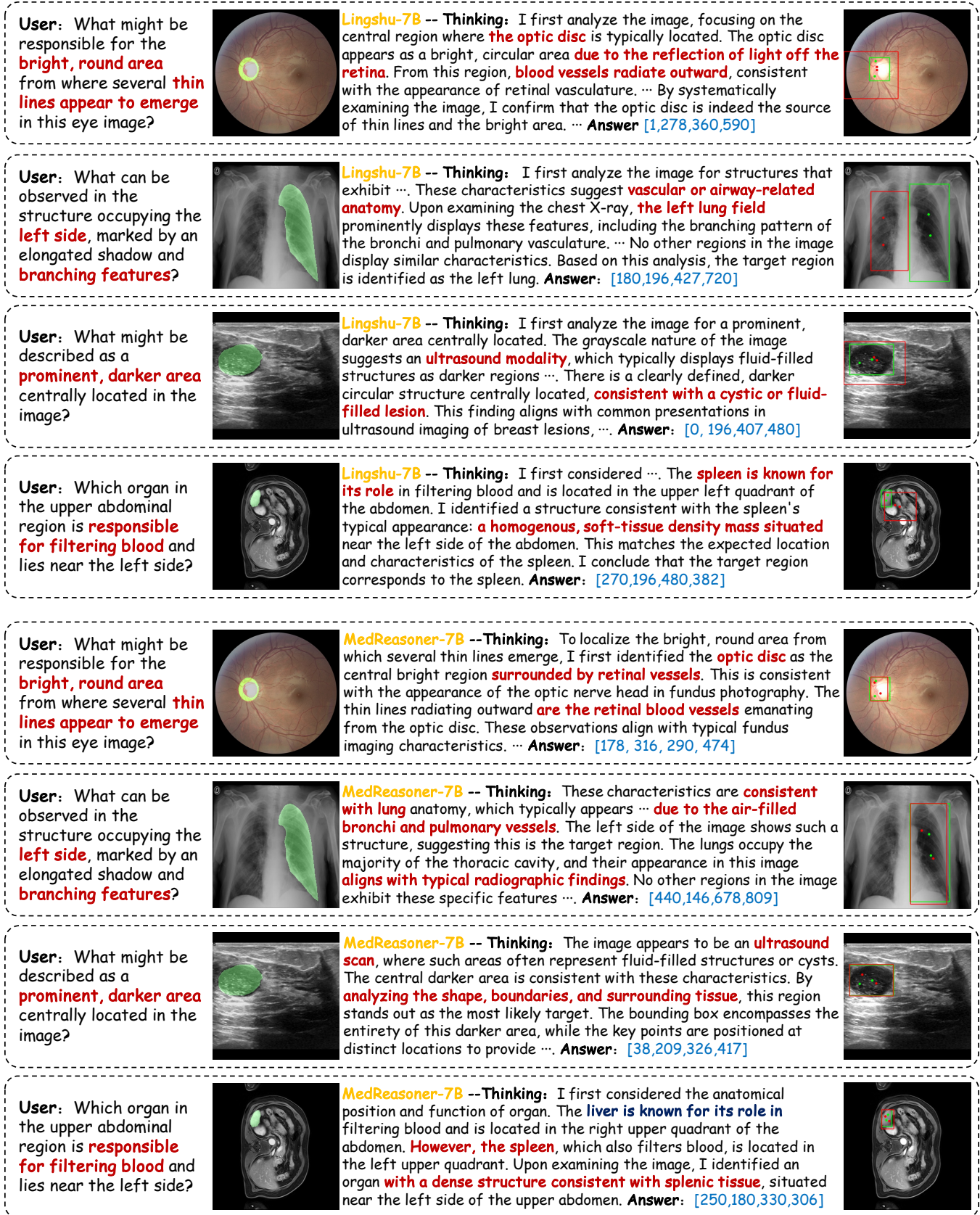
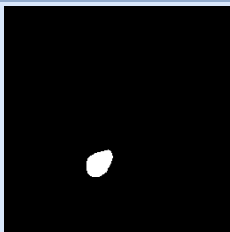
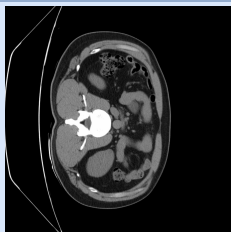


Figure 15: The top four rows show Lingshu-7B's responses in different cases, while the bottom four rows present those of ours. For each case, the columns from left to right represent the ambiguous query, the image input with the ground-truth mask, the model's reasoning process, and the model's output including the predicted bounding box and keypoints.

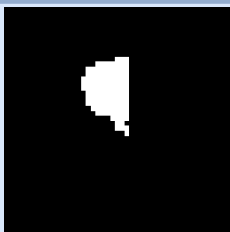
Abdomen Anatomies



modal: CT,
supercategory: abdomen anatomies,
short description: The region is an oval-shaped, smooth area on the left side of the image.,
long description: This region represents the left kidney seen in a CT scan of the abdomen, located in the lower half of the image slightly to the left of center. The kidney displays the typical biconcave, bean-like structure. The internal point positions suggest that the mass of the kidney is centered, following its characteristic shape. The kidney's overall density is homogeneous with a smooth surface texture, indicating well-defined cortical and medullary regions. Anatomically, the left kidney is positioned posteriorly, beneath the rib cage, and is surrounded by perirenal fat, which is evident in its contrast with adjacent structures. The kidney plays a crucial role in filtering blood, maintaining electrolyte balance, and excreting waste through urine.

health: Yes,
category: kidney left,

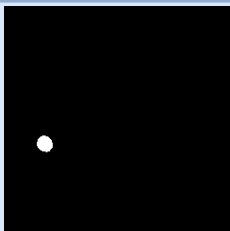
Brain Anatomies



modal: MRI,
supercategory: brain anatomies,
short description: An oval, medium-toned shape is visible towards the middle right of the image.,
long description: The highlighted region represents a portion of the posterior hippocampus, which is an essential part of the limbic system involved in memory formation and spatial navigation. In this MRI image, the region appears as a well-defined, oval structure located towards the middle right, suggesting its lateral placement in the brain. The signal intensity of this area is consistent with that of normal hippocampal tissue, appearing neither hyperintense nor hypointense relative to surrounding structures. Its smooth texture and consistent signal align with its typical appearance in MR imaging, indicating no signs of unusual tissue pathology. The posterior hippocampus is typically smaller than anterior segments, and this agrees with its proportion in the current image frame.

health: Yes,
category: posterior hippocampus,

Eye Anatomies



modal: Fundus,
supercategory: eye anatomies,
short description: A bright, circular spot in the lower-left part of the image.,
long description: This masked region represents the optic disc, a critical structure in fundus images. The optic disc is identifiable by its brighter, circular region in the lower-left quadrant of the image, where the retinal blood vessels converge and enter the eye. Its location matches typical anatomical expectations, close to the nasal side of the retina. The structure serves as the exit point for retinal nerve fibers and lacks photoreceptors, making it a natural blind spot. The optic disc's prominence and brightness are consistent with its role as the entry point for the optic nerve, crucial for visual signal transmission to the brain. In this image, its appearance is standard, with no abnormalities such as swelling or pallor visible.

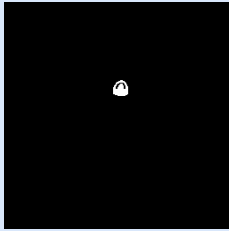
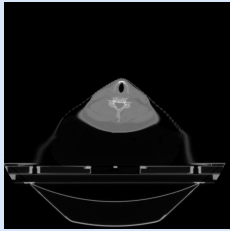
health: No,
category: posterior hippocampus,

Figure 16: Examples of the meta information from three anatomical super-categories. From top to bottom: **Abdomen Anatomies**, **Brain Anatomies**, **Eye Anatomies**. Each case presents the image along with its: *modal*, *health*, *super-category*, *category*, *short description* and *long description*.



Figure 17: Examples of the meta information from three anatomical super-categories. From top to bottom: **Lung**, **Heart Anatomies**, **Neck Anatomies**. Each case presents the image along with its: *modal*, *health*, *super-category*, *category*, *short description* and *long description*.

Neck Anatomies



modal: CT,

supercategory: neck anatomies,

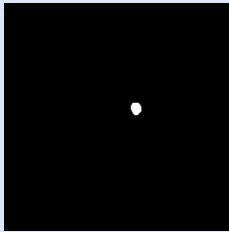
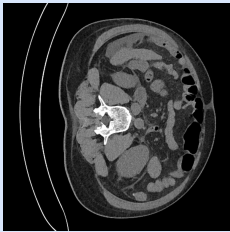
short description: The highlighted region is a small, centrally located, bright, and rounded area in the upper part of the image.

long description: This CT image represents a slice of the neck centered on the larynx, identifiable by the mask covering the highlighted area. The region is centrally located in the upper half of the image, indicating it is near the middle portion of the neck. The brightness and consistent density of the structure suggest the presence of cartilaginous tissue, typical of the larynx, which supports its role in protecting the airway and facilitating phonation. Within the mask, the shape appears rounded with a slight vertical elongation, characteristic of the laryngeal structure. The boundaries are fairly smooth, indicative of the homogeneous nature of cartilaginous structures in a healthy larynx.

health: Yes,

category: larynx,

Vessel



modal: CT,

supercategory: vessel,

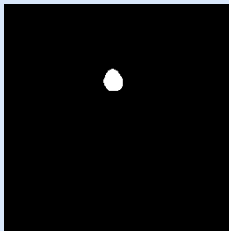
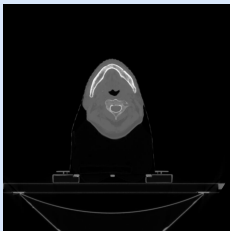
short description: Centrally located, the region appears as a smooth, tubular gray structure.

long description: The masked region in the CT image represents the inferior vena cava (IVC), commonly referred to as the postcava. It is a tubular, elongated structure centrally located, slightly to the right within the abdominal cavity. This structure is characterized by its uniform gray density, which is typical of blood vessels in CT imaging, indicating blood flow. The IVC is an important vessel, returning deoxygenated blood from the lower body to the heart, and is located anterior to the vertebral column and posterior to the liver. In this image, the IVC's position and shape appear typical, without any indication of abnormal dilation or compression. This appearance is consistent with its normal function in the circulatory system, transporting blood efficiently without obstruction or anomaly.

health: Yes,

category: postcava,

Oral Anatomies



modal: CT,

supercategory: oral anatomies,

short description: This is a centered, oval area with a uniform appearance, located in the lower middle part of the image.

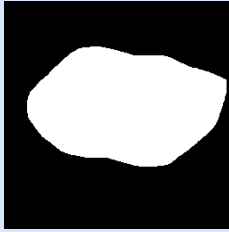
long description: The highlighted region is centrally located within the cross-sectional CT image of the head and neck, specifically within the oral cavity. The shape appears roughly oval and is situated towards the bottom half of the image, indicative of the tongue or a similar midline structure given its appearance and position. The region shows homogeneous density, consistent with soft tissues seen on CT. In the context of the oral cavity, this would align with the typical appearance of muscular structures. As part of the oral cavity, this area plays a role in functions such as speech and swallowing, interacting with surrounding anatomical structures like the mandible and other oral tissues. The substantial size and central location suggest that it might be the tongue or closely related tissue.

health: Yes,

category: oral_cavity,

Figure 18: Examples of the meta information from three anatomical super-categories. From top to bottom: **Skeletal Anatomies**, **Vessel**, **Oral Anatomies**. Each case presents the image along with its: *modal*, *health*, *super-category*, *category*, *short description* and *long description*.

Neoplasm



modal: Ultrasound,

supercategory: neoplasm,

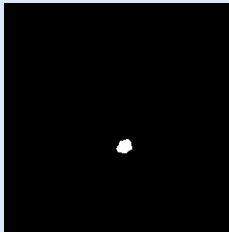
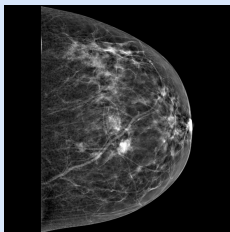
short description: The image shows a centrally located, somewhat irregular, and varied gray area with defined edges.

long description: This ultrasound image shows a single, prominent region identified within the breast tissue, consistent with a benign tumor. The mass is centrally located and presents with a mixed echogenicity, combining areas of both hypoechoic and isoechoic tissue, which is typical for such lesions. Its shape appears somewhat irregular, yet it maintains defined borders, a feature suggestive of a benign nature in breast neoplasms. The surrounding architecture is slightly compressed but maintains an overall organized pattern, indicating no invasive growth. While evaluating breast lesions, the echotexture and defined shape are crucial in distinguishing between benign and malignant conditions.

health: No,

category: neoplastic cells,

Non-neoplasm



modal: Digital Mammography,

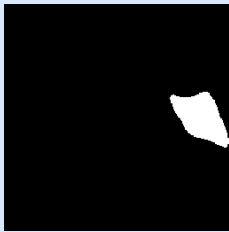
supercategory: non-neoplasm,

short description: A small, bright, irregularly shaped area is located in the lower central part of the breast tissue, appears as a small, bright, irregularly shaped mass. The lesion shows a higher density compared to surrounding fibroglandular tissues, displaying brighter intensity against the typical gray background seen in mammographic images. Its irregular shape and higher density are characteristic features often evaluated in mammography for potential pathological significance. The texture appears more granular and disorganized compared to the smoother texture of surrounding tissues, a visual cue that warrants further clinical correlation. Despite its small and localized appearance, the lesion characteristics should be carefully assessed.

health: No,

category: breast lesion,

Infection



modal: X-ray,

supercategory: infection,

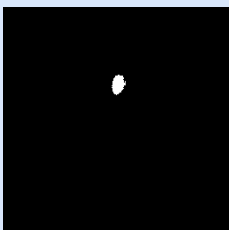
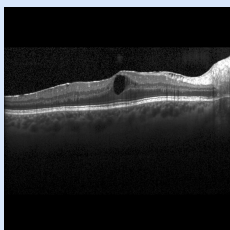
short description: A bright, irregular area appears in the upper left part of the chest,

long description: In the X-ray image, Region 1 is located on the upper left area of the lungs. It appears as a dense, somewhat irregularly shaped region, consistent with increased opacity typically seen in the context of an infection. This opacity may correspond to consolidation, often observed in cases of lung infections such as COVID-19 pneumonia. Its significant size and position suggest it may represent a prominent area of involvement. The opacity is relatively uniform, indicative of a region where alveolar spaces may be filled with fluid or cellular debris.

health: No,

category: COVID 19 infection,

Fluid Abnormality



modal: OCT,

supercategory: fluid abnormality,

short description: There's an oval, dark spot in the middle of the image, creating a smooth indentation.,

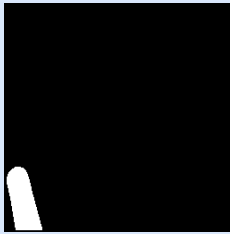
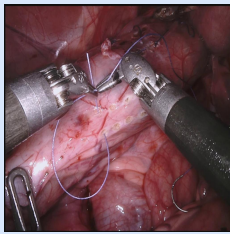
long description: In this OCT image, there is a well-defined hyporeflective area located in the outer retina, significantly affecting the integrity of the surrounding layers. The region is centrally positioned relative to the fovea, characterized by an oval shape and distinct smooth borders. This area represents an intraretinal fluid accumulation, which is often associated with conditions such as cystoid macular edema. The lesion appears to slightly displace the surrounding retinal tissue, suggesting fluid buildup that is typical of edema. This observation is consistent with the clinical picture of edema, which can lead to visual disturbances due to distortion and thickening of the retinal layers.

health: No,

category: edema,

Figure 19: Examples of the meta information from four lesions super-categories. From top to bottom: **Neoplasm**, **Non-Neoplasm**, **Infection**, **Fluid Abnormality**. Each case presents the image along with its: *modal*, *health*, *super-category*, *category*, *short description* and *long description*.

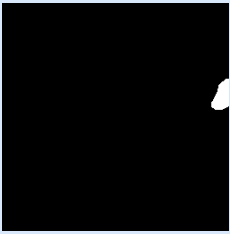
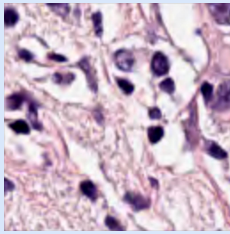
Surgical Instrument



modal: Endoscopy,
supercategory: surgical instrument,
short description: In the lower-left corner, a shiny, metal tool with a smooth, elongated shape is visible.
long description: The highlighted region shows a section of the Prograsp Forceps, a surgical instrument used in laparoscopic procedures to manipulate tissue with precision. This tool appears on the left side of the image, predominantly occupying the lower-left corner. It has a metallic, elongated shape with a smooth surface that reflects light, indicating its polished metal construction. Notable features include the jaws of the forceps, which are partially open, suggesting they are in use during the procedure, likely assisting in suturing or tissue manipulation. The region's visual characteristics match what is expected from typical laparoscopic surgical instruments.

health: No,
category: prograsp forceps,

Histology Structure



modal: Pathology,
supercategory: heart anatomies,
short description: A cluster of dark, round cells in the right corner that stand out from the background.
long description: This region is located in the lower right part of the image and exhibits several features characteristic of neoplastic cells. It appears as a densely packed group of round to oval cells with prominent nuclear features, suggesting high cellularity typical of neoplastic processes. The staining intensity is relatively uniform, indicative of the high nucleus-to-cytoplasm ratio seen in tumor cells. The arrangement of these cells shows a lack of normal tissue architecture, providing evidence of neoplastic growth within the breast tissue. This set of cells is distinguished from other areas by its concentrated appearance and distinct cellular boundaries, contributing to the categorization as neoplastic cells linked to potential malignant processes.

health: No,
category: neoplastic cells,

Figure 20: Examples of the meta information from two other super-categories. From top to bottom: **Surgical Instrument**, **Histology Structure**. Each case presents the image along with its: *modal*, *health*, *super-category*, *category*, *short description* and *long description*.

Abdomen Anatomies

The abdomen anatomies supercategory involves the structural features of numerous abdominal organs and tissues, such as solid organs like the liver, gallbladder, pancreas, spleen, and kidneys, as well as hollow organs like the gastrointestinal tract.

Question: Can you find the structure that contributes to digestion and often lies beneath another major organ?

Answer: To localize this vague area, start by identifying the central part of the image where major digestive organs are typically positioned. Look for an elongated structure that sits below another large, dense organ, which often occupies the right upper quadrant of the abdomen. This structure should have a vertical orientation and may be involved in digestion. Focus on its immediate vicinity for accompanying ducts or tubes that could confirm its identity.

Question: Which areas in the image appear as a network of loops that might handle the absorption process?

Answer: Evaluate the image for a series of looped, hollow structures usually found occupying the central and lower abdomen. Pay attention to the arrangement and how these structures form circular or semi-circular looping patterns. Tracking their continuity will help identify their extent and function. Surrounding fatty tissues and other organs can provide additional spatial cues.

Brain Anatomies

The brain anatomies supercategory provides a detailed description of various regions and structures within the brain related to key functions such as emotions, life support, and memory.

Question: Where would you find the part that's possibly affecting emotional responses in this scan?

Answer: To locate the area that may be related to emotional processes, examine regions within the limbic system. Evaluate structures at the medial aspect of the temporal lobes and look for signals that deviate from the normal signal intensities typical of gray matter. Determine the boundaries by identifying surrounding white matter tracts to discern possible involvement.

Question: Can you point out the brain area that controls basic life functions on this image?

Answer: Start by identifying the general layout of the brain, ensuring you account for the symmetrical structures. Once done, focus on the small nodal areas within the brainstem. Use horizontal sections to find areas marked by distinct signal intensity that reflect cranial nerve pathways.

Eye Anatomies

The eye anatomies supercategory describes the structures related to vision in the eye, including the shape and function of tissues such as the cornea, lens, and retina.

Question: Can you pinpoint the portion of the eye where changes in brightness are most pronounced?

Answer: To determine the specific area responsible for brightness changes, examine the ocular region for noticeable differences in signal intensity. Consider variations in the central section relative to surrounding tissues, as well as typical symmetrical presentations between both eyes.

Question: Which part of the eye is typically involved in refracting light?

Answer: Inspect the image for a lens-like structure situated centrally and projecting anteriorly. Identify the area based on its clear curvature and lens-shaped morphology distinguishing it from neighboring flat or circular regions.

Figure 21: Examples of QA formats from three anatomical super-categories. From top to bottom: **Abdomen Anatomies**, **Brain Anatomies**, **Eye Anatomies**. Each case illustrates the intended meaning of the super-category and presents two distinct QA formats for it.

Lung

The lung supercategory describes the structures related to respiratory function within the lungs, including the morphology and function of the bronchial tree, alveoli, and blood vessels.

Question: Could you point out where there might be an imbalance causing discomfort in the chest?

Answer: To locate the area mentioned, start by reviewing the left and right zones of the thorax on the scan. Focus on the delineations and symmetry, paying attention to the spaces above the diaphragm and below the collarbones. Notice regions with changes in density or any structures deviating from the expected symmetry, and observe differences in size or position compared to anatomical norms.

Question: Where is the central part that could affect breathing if it's shifted?

Answer: Examine the midline structures, focusing on any deviations toward one side. Identify the clear columnar pathways seen in cross-sectional views, observing any asymmetries or angulations. Assess the airways for any narrowing or displacement caused by pressure differences or external mass effect

Heart Anatomies

The heart anatomies supercategory covers a detailed description of various structures of the heart, including key components such as the heart chambers, myocardium, and heart valves.

Question: Could you point out the more solid-looking pointy edge within the center of the chest image?

Answer: When approaching the center of the chest on an axial view of the heart, you would first identify the left and right sides. Focus on the side opposite the largest dark chamber. From here, locate the area just above this dark region, recognizing that this structure forms the anterior wall. This anterior structure should be encased more densely and is crucial in forming the heart's muscular contour.

Question: Where might you find the circular dense region that's almost in the middle but leans to one side?

Answer: Begin by locating the central split between the left and right sides of the chest image. Focus on the dense, circular structure that appears centrally but slightly shifted towards the left. This structure is thicker, and its walls are consistently denser than other surrounding structures. It's often more centrally located in relation to major vessels that go upward.

Neck Anatomies

The neck anatomies supercategory involves the structural features of numerous organs and tissues in the neck, including the thyroid gland, trachea, esophagus, and major blood vessels.

Question: Can you point out the area that's looking a bit puffed in this neck region?

Answer: Begin by examining the anterior region of the neck, where a prominent curve or protrusion may be visible. Look for symmetry or any shifts from the midline that could indicate swelling. Pay attention to the contour and surface texture, as these may help in identifying the specific anatomical structure. Evaluate any deviations from typical anatomy, which may provide further indicators of the organ involved.

Question: What could be that slender passage-like area in this image?

Answer: Focus on the central vertical axis of the neck, considering what structures normally appear here. Compare the density and uniformity of this region to surrounding areas, which may assist in locating the target. Examine the alignment with other known landmarks or anatomical anchors in this area to distinguish the observed shape.

Figure 22: Examples of the meta information from three anatomical super-categories. From top to bottom: **Lung**, **Heart Anatomies**, **Neck Anatomies**. Each case illustrates the intended meaning of the super-category and presents two distinct QA formats for it.

Skeletal Anatomies

The skeletal anatomies supercategory provides a detailed description of the structural features of the skeletal system, including the shape and function of bones and joints.

Question: Where might you locate the part that looks like a central connecting point and seems slightly different on each side?

Answer: Begin by examining the overall geometry of the bones, especially focusing on the natural curvature and alignment as seen in an X-ray or MRI. Look for consistent bilateral symmetry across the image, and trace any divergence that leads to a vertical division, likely indicating the target zone. Typically, you will need to assess areas where major bones connect and identify the concatenating points amidst the skeletal framework. Following these observations, determine the central location of the junction, which is indirectly implied by its spatial prominence and supportive role in bodily centre of gravity.

Question: Can you tell where the section that mirrors itself and bends gracefully within the body might be?

Answer: Use a panoramic view, such as a full-body scan, to identify the torso region and zoom in on vertically aligned structures. Notice the shape symmetry with mirror-image alignment and any curvature that forms naturally in contrast to adjacent tissues. Observe structural densities depicting clear sharp lines in radiography, focusing on zones with visibly distinct borders indicative of functional articulation points. This will help you isolate the target feature where the edges converge and align.

Vessel

The vessel supercategory describes the morphological characteristics of the vascular system, including the branching and narrowing of arteries and veins.

Question: Can you find the place in the image where the main pathways distribute nutrients all over the region?

Answer: To locate the area described, observe the image for tubular structures, often with branching patterns, originating from a central hub or core. Look for these structures where they serve a major transport role, possibly interfacing with the central part of the body. Evaluate differences in intensity or size where the tubular structures meet the larger central mass, as this may mark the functional transition zone. This method will help identify key vessel junctions or branches in the image and guide you to the described region.

Question: Where in the image is the area that seems to pulse steadily, sending things all around?

Answer: In identifying this region, start with the central pulsating structure in the image, which is usually the core source of rhythmic flow indicators. Follow the consistently repeating patterns that spread outward from it, reflecting a regular and rhythmic architecture. Assess the space where these patterns start interfacing with smaller domains or change significantly in width, which often symbolizes a shift in function or hemodynamic pressure. Such cues are typical indicators of major vessel entry points or exits in the visual scan.

Oral Anatomies

The oral anatomies supercategory describes the structures in the oral cavity related to functions such as chewing, swallowing, and speech, including teeth, tongue, and salivary glands.

Question: Can you locate the area that is crucial for both speaking and breathing?

Answer: To pinpoint this target, first focus on the central region of the oral cavity. Observe the structures that are aligned with pathways for air passage and speech formation, typically situated towards the anterior section. Identify symmetric formations which help define the boundaries. The surrounding areas should display distinctions in texture and density from neighboring tissues, marking them as separate functional entities.

Question: Where is the spot that plays a key role in chewing and saliva production?

Answer: Begin by examining the lateral aspects of the oral cavity for symmetrical bulges. These structures are normally present in pairs, positioned laterally corresponding to each side of the face. Their texture can be identified as different from the surrounding muscle tissue, displaying a more homogeneous appearance. Consider the implications for mastication and secretory functions, which are often associated with these structures.

Figure 23: Examples of the meta information from three anatomical super-categories. From top to bottom: **Skeletal Anatomies**, **Vessel**, **Oral Anatomies**. Each case illustrates the intended meaning of the super-category and presents two distinct QA formats for it.

Neoplasm

The neoplasm supercategory covers the characteristics of tumors on imaging, including their impact on surrounding tissues and metabolic properties.

Question: Where is the area that impacts control and coordination most likely located?

Answer: To locate the region affecting control and coordination, examine the areas within the image where neural pathways are prominent. Look for anomalies in the density or arrangement that might suggest interference with typical neural functions. These might appear as irregularities or disruptions in the uniformity of the tissue.

Question: Can you identify where the region that affects metabolic rate will be?

Answer: Find the site by observing areas where the tissue density is significantly altered, suggesting a change in metabolic activity. These areas often appear as regions with unusual signal intensity or enhancement patterns, indicating potential abnormal growth impacting metabolic functions.

Non-neoplasm

The non-neoplasm supercategory describes the imaging characteristics of non-neoplastic lesions, including abnormal density and signal patterns.

Question: Could you point out the area that looks like it doesn't belong with the rest?

Answer: Guide your attention to regions where tissue contrasts sharply with surrounding structures, focusing on areas that are irregularly shaped or appear denser than expected in nearby regions. Use variations in intensity among adjacent tissues to hone in on slight abnormalities. Pay attention to any spatial asymmetry relative to normally regular patterns.

Question: Which part seems to disrupt the normal flow or pattern in this image?

Answer: Emphasize exploring zones that are subtly interrupting natural flow lines or layering noticeable in healthy structures. Look closely at spots where the contrast enhancement fluctuates slightly against an expected uniform background. Irregularity in surface or border definition will help in guiding towards the area in question.

Infection

The infection supercategory involves abnormal areas within the body caused by infections, including the morphological characteristics of pathological changes such as inflammation and abscesses.

Question: Can you identify the area in the image that might be working harder than usual?

Answer: Start by observing areas within the image that exhibit increased brightness in relation to surrounding tissues, as these are often indicative of an active physiological processing region. Focus on understanding how this might relate to the overall structure, ensuring to consider any characteristic patterns of symmetry or surrounding tissue involvement.

Question: Where in the image might there be an irregular shape that doesn't fit?

Answer: Consider regions where the shape appears inconsistent or irregular relative to typical anatomical structures. This disparity may suggest an abnormality, especially if accompanied by uneven texture or unexpected convergence of otherwise distinct boundaries.

Fluid Abnormality

The fluid abnormality supercategory involves areas within the body where there are abnormal fluid accumulations or density changes, indicating potential pathological conditions such as edema, effusion, or hemorrhage.

Question: Can you find where there seems to be a concentration of something denser or lighter than the surrounding tissues?

Answer: To find this location, first analyze the images for any areas that appear less opaque than surrounding tissues, which may suggest the presence of fluid. Look for these areas in places where fluid may accumulate, such as dependent regions or spaces between organs. Consider the shape and boundary of this opacity, as fluid collections often adapt to surrounding anatomical structures. Anomalies may also show different densities or intensities compared to normal tissue.

Question: Which part of the eye is typically involved in refracting light?

Answer: Begin by identifying regions that appear more prominent or swollen compared to adjacent areas, which can be indicative of fluid accumulation. Focus on anatomical boundary distortions or elevations in specific regions. Check for differences in texture or contrast, as these variations can signify the presence of fluid. Pay attention to changes in the consistency of tissues, where fluid would create a more homogenous appearance compared to normal heterogeneity.

Figure 24: Examples of the meta information from four lesions super-categories. From top to bottom: **Neoplasm**, **Non-Neoplasm**, **Infection**, **Fluid Abnormality**. Each case illustrates the intended meaning of the super-category and presents two distinct QA formats for it.

Surgical Instrument

The surgical instrument supercategory covers the imaging characteristics of various surgical instruments used during surgical procedures, helping to identify the interaction between instruments and tissues.

Question: Which object in the image seems to be interacting closely with nearby structures?

Answer: To identify the tool causing this interaction, look for a thin, elongated object with metallic properties, usually reflecting light distinctly from surrounding tissues. It is typically found near the area of manipulation, such as near connective structures or regions with visible incision marks.

Question: What object has a joint-like appearance that seems separate from denser tissues?

Answer: Identification starts by looking for an object with a peculiar handle situated away from patient anatomy but near the incision area. This object often appears slightly detached from denser tissues and might have moving joint parts visible under the imaging modality.

Histology Structure

The histology structure supercategory describes the arrangement and morphological characteristics of tissues such as cells, glands, and blood vessels, reflecting the normal or pathological state of the tissues.

Question: Can you find the section where one type of cell transitions to another?

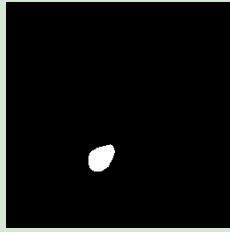
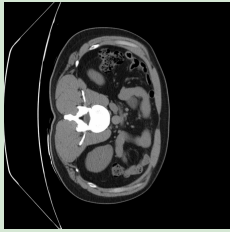
Answer: Start by observing the overall architectural pattern of the tissue. Look for regions where the cells are narrowly aligned, suggesting a boundary or interface. Identify any linear arrangement of nuclei or a darker coloration demarcating a transition. Once the boundary-like features are located, verify their continuity and relation to adjacent tissue structures.

Question: Where can you see a crowded group of cells that might look distinct from the rest?

Answer: First, identify areas where the cell density varies significantly. Look for regions with a higher concentration of smaller, rounder cells. Examine their organization and clustering patterns, as these areas often appear more densely packed than others. Confirm this by comparing their appearance with neighboring less congested regions.

Figure 25: Examples of the meta information from two other super-categories. From top to bottom: **Surgical Instrument**, **Histology Structure**. Each case illustrates the intended meaning of the super-category and presents two distinct QA formats for it.

Abdomen Anatomies



modal: CT,
supercategory: abdomen anatomies,

health: Yes,
category: kidney left,

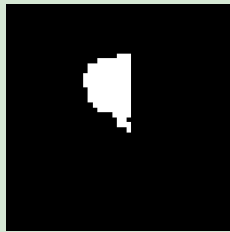
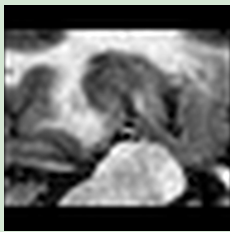
question: What structure appears as a light, smooth oval on the left side of the abdomen in this image?

think: The region in focus shows a smooth, oval structure on the left side of the abdomen, appearing as a lighter area compared to its surroundings. This is typical of a kidney, commonly located posteriorly under the rib cage. Its homogeneous density and clearly defined borders are indicative of well-delineated cortical and medullary regions. Anatomically, it fits the characteristic shape and position of the left kidney relative to other abdominal organs. Therefore, this region is the left kidney, consistent with its normal anatomical presentation in the image.

bbox: [372,644,491,767]

point: [[421,713],[452,685]]

Brain Anatomies



modal: MRI,
supercategory: brain anatomies,

health: Yes,
category: posterior hippocampus,

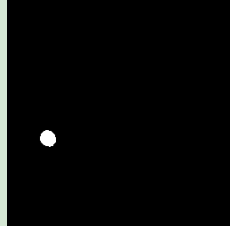
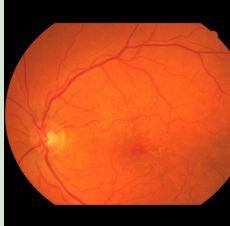
question: How might one focus on regions that are crucial for processing spatial and memory-related information in this brain imaging?

think: The highlighted area demonstrates a well-defined oval shape positioned towards the middle right of the image, suggesting it belongs to the limbic structures. The consistent signal intensity and smooth texture confirm that it corresponds to the typical appearance of this region in the brain, indicating no abnormalities. The structure's lateral placement aligns with the posterior section of a memory-related brain area. This identification is consistent with known anatomical location and proportions, notably for structures involved in memory and spatial navigation.

bbox: [348,224,563,579]

point: [[464,352],[505,435]]

Eye Anatomies



modal: Fundus,
supercategory: eye anatomies,

health: No,
category: optic cup,

question: What is the bright circular area where the eye's structures seem to converge located?

think: The indicated region is identified by a bright, circular spot in the lower-left part of the image, distinct from surrounding retinal tissue. This observation corresponds with the optic disc, where retinal blood vessels converge. The brightness and central convergence of vessels confirm its role as the point where the optic nerve exits the eye. Its circular shape and position, relative to the nasal side of the retina, align with typical features of the optic disc. This description guides us to conclude the masked region is indeed associated with the optic disc area.

bbox: [148,584,219,659]

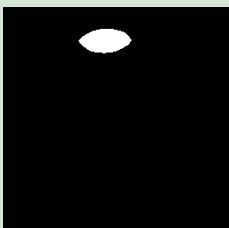
point: [[183,621],[207,630]]

Figure 26: Examples of the QA pairs from three anatomical super-categories. From top to bottom: **Abdomen Anatomies**, **Brain Anatomies**, **Eye Anatomies**. Each case presents the image along with its: *modal*, *health*, *super-category*, *category*, *question*, *think*, and *answer* (*bbox*, *point*).



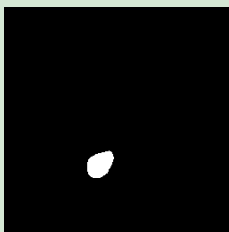
Figure 27: Examples of the QA pairs from three anatomical super-categories. From top to bottom: **Lung**, **Heart Anatomies**, **Neck Anatomies**. Each case presents the image along with its: *modal*, *health*, *super-category*, *category*, *question*, *think*, and *answer* (*bbox*, *point*).

Skeletal Anatomies



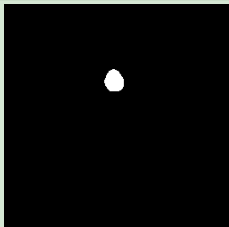
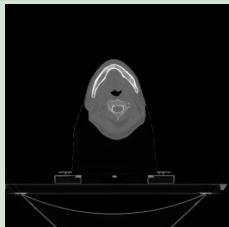
modal: Ultrasound, **health:** No,
supercategory: skeletal anatomies, **category:** pubic symphysis,
question: What structural features can be observed along the upper midline in this region of the ultrasound image?
think: The highlighted region corresponds to a structure that is centrally positioned in the upper part of the image, appearing as a consistent bright area due to its interface with dense material. This location is typical for a critical junction in the skeletal anatomy, noted for its prominence and central role. The structure's elongated and smooth texture is characteristic of a major bony interface that unites portions of a larger framework. Based on these observations, the region is identified as the pubic symphysis, which is central and midline in the context of pelvic skeletal components, distinguished by its echogenic appearance.
bbox: [340,100,579,211] **point:** [[455,154],[511,151]]

Vessel



modal: CT **health:** Yes,
supercategory: vessel **category:** postcava
question: What is the elongated central structure just right of the midline in the image?
think: The region can be identified by its central location slightly to the right within the abdominal cavity. It's characterized by its smooth and tubular appearance, which aligns with the typical presentation of major blood vessels on a CT image. This vessel is found anterior to the vertebral column, indicating its relationship with the rest of the body's vascular network. It returns deoxygenated blood from the lower body to the heart, functioning efficiently as seen by its consistent gray density. This appearance matches the expected anatomy and position of the inferior vena cava.
bbox: [572,448,619,503] **point:** [[597,475],[587,459]]

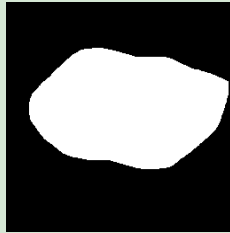
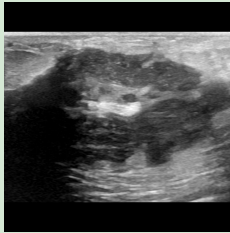
Oral Anatomies



modal: CT, **health:** Yes,
supercategory: oral anatomies, **category:** oral cavity,
question: Which structure in the lower part of the cross-section plays a crucial role in oral functions?
think: To identify the central structure within the image, focus on the lower half where a uniform, soft tissue density is visible. This area appears oval in shape and is located centrally towards the bottom of the cross-section. Given the homogeneous appearance typical of muscle, it functions primarily in speech and swallowing. Its position and texture suggest it is a key component of the oral cavity, likely corresponding to the tongue. This conclusion is supported by its size and central location within the oral anatomical region.
bbox: [448,292,535,391] **point:** [[494,351],[489,318]]

Figure 28: Examples of the QA pairs from three anatomical super-categories. From top to bottom: **Skeletal Anatomies**, **Vessel**, **Oral Anatomies**. Each case presents the image along with its: *modal*, *health*, *super-category*, *category*, *question*, *think*, and *answer (bbox, point)*.

Neoplasm



modal: Ultrasound,

supercategory: neoplasm,

question: In this image, what area might show distinctive structural characteristics within the tissue?
think: In the ultrasound image, the irregularly shaped structure with mixed echogenicity is a key feature. It is centrally located and its somewhat defined borders help to distinguish it from the surrounding tissue. The combination of hypoechoic and isoechoic areas supports identification of this as a benign tumor within breast tissue. Observing the organized surrounding architecture and lack of invasive appearance further verifies the region as benign. These characteristics collectively confirm the area corresponds to the highlighted segment and its benign nature.

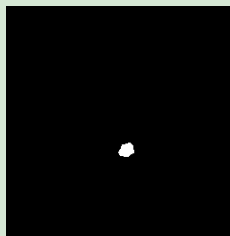
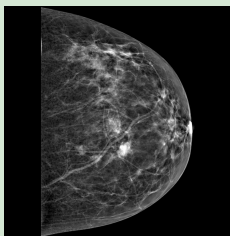
bbox: [104,204,1003,743]

health: No,

category: benign tumor,

point: [[643,493],[405,464]]

Non-neoplasm



modal: Digital Mammography,

supercategory: non-neoplasm,

question: What area shows different textural characteristics compared to surrounding breast tissue?

think: The target region is identified by its distinct brightness and irregular shape, distinguishing it as a focal area of interest. Located in the lower central portion of the breast, this area stands out against the typical gray background of the surrounding tissues due to its higher density. The irregular mass contrasts sharply with the smoother contours of neighboring parenchyma, guiding attention to this specific region. Its appearance is quite bright and small, which, in the context of a mammographic image, signifies a characteristic worth closer examination. Thus, the visual cues lead directly to the target within the marked boundaries of interest, indicating its clinical relevance.

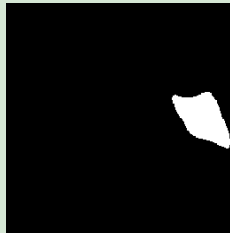
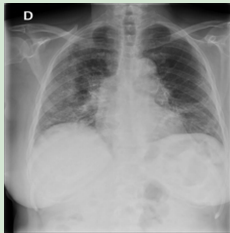
bbox: [504,608,575,671]

health: No,

category: breast lesion,

point: [[541,641],[521,653]]

Infection



modal: X-ray,

supercategory: infection,

question: What area seems to present an unusual brightness in the chest region on this X-ray?

think: The region in question is located in the upper left area of the lungs, noticeable for its increased density on the X-ray. It stands out due to its brightness compared to surrounding lung tissue, suggesting an area of increased opacity. The shape is somewhat irregular but well-defined, occupying a prominent portion of the lung field. This feature suggests it may be an area where the normal lung aeration is decreased, possibly due to consolidation. By evaluating its size and positioning within the thoracic cavity, its characteristics align with where pathological changes like infections are typically noted.

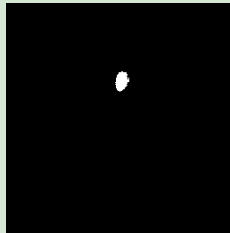
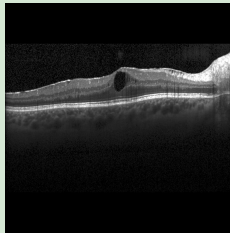
bbox: [144,104,475,583]

health: No,

category: COVID-19 infection,

point: [[313,399],[302,284]]

Fluid Abnormality



modal: OCT,

supercategory: fluid abnormality,

question: What could cause an indentation in this area of the eye on the image?

think: The region of interest is identified by a distinct darkened oval area within the retinal layers, centrally positioned and smoothly defined. This area disrupts the continuity of the otherwise uniform retinal layers, indicating a notable space filled with fluid. Its placement suggests a buildup internal to the retinal structure, affirming it as an area where fluid accumulation is prominent. The smooth curvature and displacement of adjacent tissue mark the defined nature of this swelling, characteristic of conditions causing fluid retention within the retina.

bbox: [492,304,555,395]

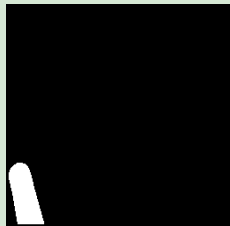
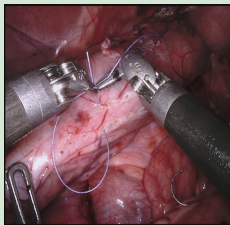
health: No,

category: edema,

point: [[522,345],[515,370]]

Figure 29: Examples of the QA pairs from four lesions super-categories. From top to bottom: **Neoplasm**, **Non-Neoplasm**, **Infection**, **Fluid Abnormality**. Each case presents the image along with its: *modal*, *health*, *super-category*, *category*, *question*, *think*, and *answer* (*bbox*, *point*).

Surgical Instrument



modal: Endoscopy,

supercategory: surgical instrument,

question: What instrument appears to be actively holding or repositioning tissue in this view?

think: Upon examining the image, noticeable near the lower-left corner is a shiny, metallic tool with a distinct smooth, elongated form, engaged in handling or positioning soft tissues. The tool's polished surface reflects light, confirming its metallic construction. Its operational design, featuring partially open jaws, implies interactive use during a laparoscopic procedure. This configuration suggests the tool's role in suturing or manipulating tissues, characteristic of surgical instruments. Such a description aligns with that of forceps used to precisely handle and adjust tissues during minimally invasive surgeries.

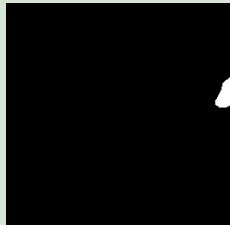
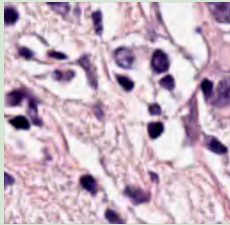
bbox: [12,732,171,1015]

health: No,

category: prograsp forceps,

point: [[99,960],[82,879]]

Histology Structure



modal: Pathology,

supercategory: histology structure,

question: Which area in image shows a more clustered and unique cell structure compared to the rest?

think: The highlighted area is in the lower right section of the image. You can recognize it by examining the cellular organization where a dense cluster of small, round to oval cells stands out distinctly from the surrounding area. This grouping lacks the typical tissue architecture expected in other regions, with cells appearing tightly packed together with pronounced nuclei. Contrast it with the less densely populated and more disorganized cells in neighboring sections to confirm its nature as a focal point of interest.

bbox: [944,340,1023,479]

health: No,

category: neoplastic cells,

point: [[1023,410],[986,444]]

Figure 30: Examples of the QA pairs from two other super-categories. From top to bottom: **Surgical Instrument**, **Histology Structure**. Each case presents the image along with its: *modal*, *health*, *super-category*, *category*, *question*, *think*, and *answer* (*bbox*, *point*).